

<https://doi.org/10.1038/s41529-025-00616-4>

A mesoscale phase-field model of intergranular liquid lithium corrosion of ferritic/martensitic steels



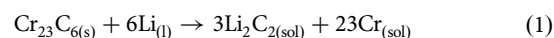
Alexandre Lhoest¹, Sasa Kovacevic², Duc Nguyen-Manh³, Joven Lim³, Emilio Martínez-Pañeda²✉ & Mark R. Wenman¹

A phase-field model is developed to simulate intergranular corrosion of ferritic/martensitic steels exposed to liquid lithium. The chromium concentration of the material is used to track the mass transport within the metal and liquid (corrosive) phase. The framework naturally captures intergranular corrosion by enhancing the diffusion of chromium along grain boundaries relative to the grain bulk with no special treatment for the corrosion front evolution. The formulation applies to arbitrary 2D and 3D polycrystalline geometries. The framework reproduces experimental measurements of weight loss and corrosion depth for a 9 wt% Cr ferritic/martensitic steel exposed to static lithium at 600 °C. A sensitivity analysis, varying near-surface grain density, grain size, and chromium depletion thickness, highlights the microstructural influence in the corrosion process. Moreover, the significance of saturation is considered and evaluated. Simulation results show that near-surface grain density is a deciding factor, whereas grain size dictates the susceptibility to intergranular corrosion.

The commercialization of fusion energy remains hindered by many overwhelming engineering problems that need addressing prior to its implementation. A key one is the feasibility of breeding tritium in situ using lithium-bearing materials. Liquid lithium (Li) provides unique benefits^{1,2}. The concern of radiation damage is eliminated as the breeder material is in a liquid state, which offers greater flexibility and efficacy in the extraction of tritium as the breeder material can circulate away from the extreme conditions of the reactor. Furthermore, the inherent efficacious thermal properties of liquid metals indicate that one can operate at higher temperatures, leading to greater thermal efficiencies^{3,4}. Several potential candidates for the optimum structural material for future fusion power plants are currently being investigated, including ferritic/martensitic (F/M) steels and vanadium-based alloys^{5–7}. Each candidate material possesses its respective advantages, yet owing to the worldwide expertise and generations of use in the fission industry, many of the proposed designs have opted for F/M steels⁸, thereby exploiting the high strength and low creep rate at elevated temperatures, plus desirable irradiation performance⁹.

A limiting concern to the implementation of liquid Li as a breeder material is the harsh corrosive environment it produces when in contact with structural alloys, ultimately leading to weight loss and surface recession (i.e., wall thinning) influencing the longevity of the structural material and heightening the risk of accumulated activated material¹⁰. The corrosion of alloys with liquid Li is solely based on physio-chemical processes, where the

principal mechanisms are solubility-driven dissolution, intergranular corrosion (IGC), and mass transfer^{11,12}. As such, the composition of the structural alloy in contact with the liquid metal is a substantial factor in the corrosion resistance, owing to the varying solubility limits of alloying elements differing by several orders of magnitude in some cases¹³. Furthermore, Li preferentially attacks grain boundaries (GBs) due to their heterogeneity, tendency for chemical segregation, and precipitation of secondary phases. The compatibility of F/M steels with liquid Li is heavily correlated with the amount of Cr in the composition of the steel¹⁴. Cr is preferentially leached from the structural alloy attributed to its comparatively heightened solubility limit^{14,15}. The amount of Cr regulates the chemical activity of carbon in the metal by forming metallic carbides (i.e., Cr₂₃C₆). Liquid Li preferentially corrodes GBs as these regions are decorated with carbides, relative to a tempered martensitic microstructure¹⁶. Once exposed to liquid Li, these carbide precipitates become unstable and are subsequently leached¹⁷ via the following reaction



resulting in a heavily chemically altered region¹⁸, commonly observed through a phase transformation of the matrix from martensite to ferrite¹⁹. Once the alloying elements in the immediate vicinity are depleted, resulting in a chemical gradient, bulk alloying elements diffuse toward the corroding

¹Imperial College London, Centre for Nuclear Engineering, South Kensington Campus, London, UK. ²Department of Engineering Science, University of Oxford, Oxford, UK. ³United Kingdom Atomic Energy Authority, Culham Campus, Abingdon, UK. ✉e-mail: emilio.martinez-paneda@eng.ox.ac.uk

interface to replenish the lost material. Although the compatibility of F/M steels with liquid Li at elevated temperatures has been experimentally explored in depth^{20,21}, showcasing its applicability, there still remains little consensus on the dominant corrosion mechanism and the principal microstructural features, that govern the corrosion process.

Evaluating IGC resistance and the long-term effects of materials exposed to liquid Li presents significant challenges due to the unique conditions of this corrosive environment. Numerical modeling can expand the reach of experimental studies by providing insights and extending the duration of experiments involving liquid Li under various conditions. Ideally, these models can guide the design of materials optimized for liquid Li environments and suggest strategies to minimize susceptibility to IGC. Modeling the corrosion resistance of structural materials has been detailed in abundance through various computational techniques, including Lagrangian-Eulerian approaches^{22,23}, peridynamics^{24,25}, cellular automata models^{26,27} and phase-field methods^{28–38}. However, these are mainly used in the context of uniform and localized corrosion and stress corrosion cracking. As such, these models are limited in capturing IGC, assessing the compatibility of liquid Li with F/M steels, and incorporating the microstructural influence on IGC. The synergistic effect of aggressive environments and underlying microstructures has been recently resolved in the context of IGC^{39–43}. Albeit these IGC models provide mechanistic predictions and insight, they do not properly resolve the differing corrosion kinetics in the grain bulk and GBs^{39–41}, a key feature of liquid Li IGC. Other models utilize multiphase-field formulations^{42,43} to distinguish between GBs, grain interiors, and the corrosive environment. However, these multiphase-field approaches inherently possess high computational costs. Moreover, neither model surveyed the correlation between microstructural properties and their influence on the IGC process. The present work aims to develop a phase-field model to assess the IGC of F/M steels in contact with liquid Li. As the underlying physical mechanics in the corrosion process, the diffusion process is differentiated between GBs and grain bulk, effectively and naturally addressing the varying corrosion kinetics while keeping the phase-field equation unaltered. An additional stationary parameter is introduced to distinguish mass transport between GBs and grain interiors, which reduces the computational cost intrinsically associated with multiphase-field formulations.

The remainder of the paper is organized as follows. The underlying corrosion mechanism of F/M steels exposed to liquid Li and the associated modeling assumptions are presented in section "Methods". The chromium (Cr) concentration of the material is used to track mass transport within the metal and liquid (corrosive) phase. The phase-field model is subsequently derived from a generalized thermodynamic free energy functional. The governing equations for the phase-field parameter and Cr concentration in

the system, as the primary variables of the model, are derived in a thermodynamically consistent way. GBs are differentiated from grain interiors using an additional independent stationary parameter that allows for incorporating representative diffusivities of Cr along GBs and grain bulk, exploiting physical material parameters to capture IGC. The constructed framework is calibrated and validated against experimental measurements on a 9 wt% Cr F/M steel in contact with static liquid Li at 600 °C in section "Model calibration and validation", demonstrating its ability to capture IGC phenomena. After validation, a sensitivity analysis for different microstructural features, including grain density at the exposed surface, grain size, and Cr depletion thickness, is performed to investigate their role in the corrosion resistance of the simulated material in section "Results". The main conclusions are subsequently discussed in section "Discussion" as well as the investigation findings and recommendations for future work.

Results

Influence of grain density at the exposed surface

The microstructures employed to calibrate the model had 6 GBs at the exposed surface. To understand the influence of grain density at the near-surface, the grain structure distribution is varied while keeping an average grain size of 20 μm . In addition to the reference geometry in section "Model calibration and validation", two further microstructures, with 5 and 7 GBs at the exposed surface, were analyzed. As previously, the average behavior was taken from ten equiaxed microstructures for each case. Figure 1 displays the representative microstructure for each scenario while the ten microstructures used for the 5 and 7 GB microstructures can be viewed in Figs. S.2 and S.3 (Supplementary Information). The resultant phase-field predictions can be seen in Fig. 2 where the standard deviation (SD) data at 100, 250, and 500 h exposure time are depicted in Fig. 3.

The weight loss data, presented in Fig. 2a, highlights a positive correlation with the number of grains at the exposed surface. The microstructures that possess 7 GBs exhibited the most significant weight loss over the 500 h simulation. Contrastingly, the microstructures with 5 GBs give rise to the lowest weight loss. Overall, all three microstructures with 5, 6, and 7 GBs at the exposed surface produce largely identical profiles, whereby the difference in weight loss between the three types of microstructures increases with increasing exposure time. As such, it is apparent during the first 500 h of exposure that the rate of weight loss is most severe for the 7 GB microstructure, resulting in a comparatively greater weight loss of 1.34 g/m^2 . The 5 GB microstructure, on the other hand, exhibits 1.01 g/m^2 of material weight loss. On average, the total weight loss after 500 h increases by $\sim 15\%$ each time increasing the grain density at the interface by a single grain. Consequently, the 7 GB microstructures overestimate the weight loss at 100 and 250 h compared to the experimental measurements. Yet, it remains

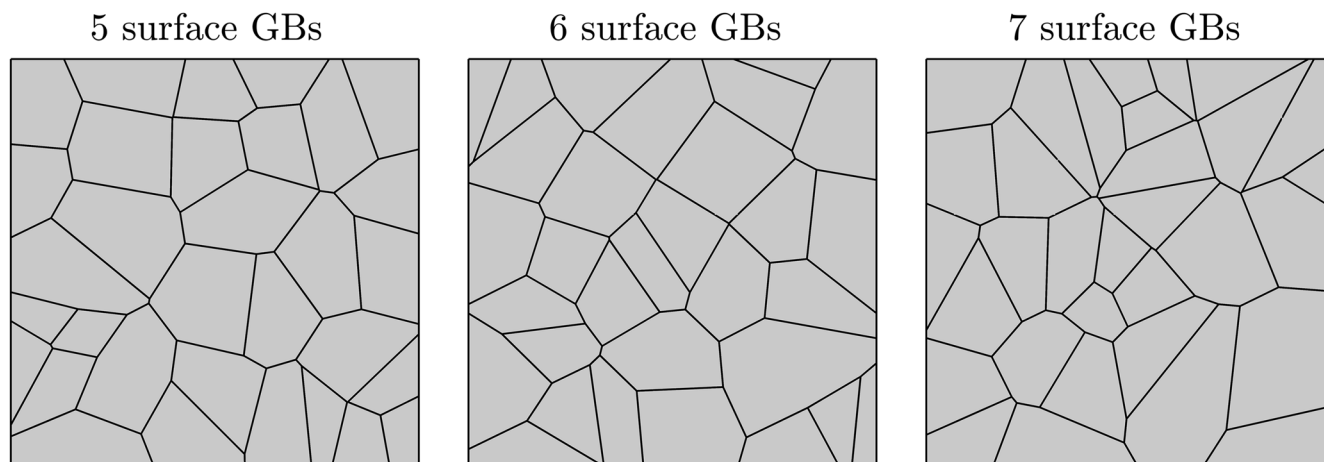


Fig. 1 | Representative microstructures for the 5, 6, and 7 surface GB microstructures simulated. Each microstructure has an average grain size of 20 μm , while varying the number of GBs at the exposed surface located at the uppermost boundary.

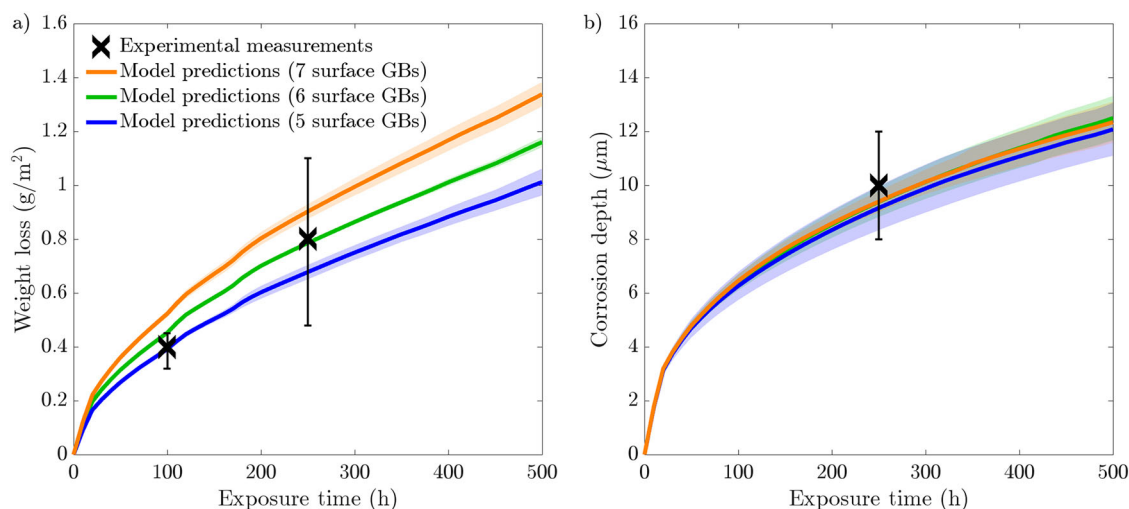


Fig. 2 | Phase-field predictions following a 500-h simulation for 20 μm average grain size microstructure with 5, 6, and 7 GBs present at the exposed surface compared to experimental measurements⁴⁴. Phase-field predictions for a weight

loss and **b** corrosion depth. The data presented for each case are taken from an average of ten microstructures where the shaded colored regions represents the SD of the ten simulations.

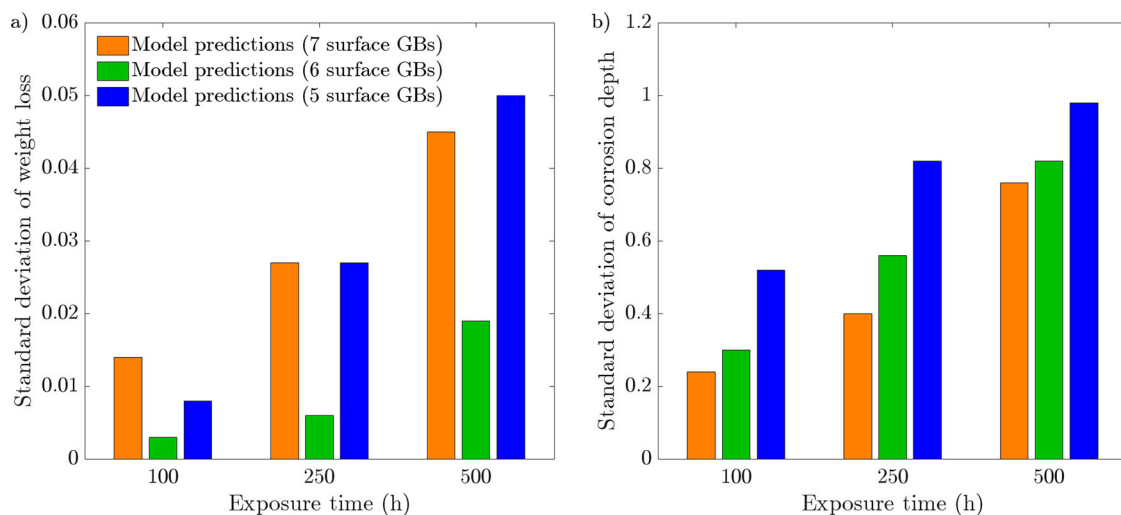


Fig. 3 | Standard deviations at 100, 250, and 500 h intervals for 20 μm average grain size microstructure with 5, 6, and 7 GBs present at the exposed surface. Standard deviations for **a weight loss and **b** corrosion depth. The data presented for each case are taken from an average of ten microstructures.**

within the relative error for the 250 h weight loss experimental measurement. Alternatively, the 5 GB microstructures predicts with a degree of high accuracy the weight loss at 100 h. However, it underestimates the weight loss at 250 h, while remaining within the relative error. Furthermore, after 500 h, the 5 and 7 GB microstructures give rise to almost identical SDs, which are more than twice as large compared to the 6 GB microstructures, Fig. 3a. The corrosion depth data displays zero influence on the near-surface grain density as all three types of grain structures give rise to predominantly identical corrosion depth profiles. Overall, the three microstructures simulated generate an average corrosion depth of 12.3 μm . Contrary to the weight loss data, the SDs regarding the corrosion depth exhibit a clear order. The 5 GB microstructures produce the greatest SD, followed by the 6 GB microstructures, where the 7 GB microstructures return the smallest SD after 500 h of exposure time, Fig. 3b.

Figure 4 shows the progression of corrosion of the representative microstructures (Fig. 1) following a 30,000 h exposure time. The onset of corrosion initiates at the GBs exposed to the liquid metal at the uppermost boundary. As time increases, the evolution of ϕ continues along the GBs deeper into the material. Congruently, Fig. 5 shows that the diminished

concentration of Cr intensifies as Li advances into the steel. The spread of concentration of Cr along the GBs indicates the corrosion process operates in the diffusion-controlled regime. The near-surface GBs are seen to be completely leached of Cr, with this process increasing in depth as time progresses. In addition, the degree of corrosion regarding the near-surface GBs visibly heightens, as seen through the increased thickness of the $\phi = 0$ region. In some instances, two corrosion fronts are seen advancing at either end of the same GB, where they ultimately meet, engulfing the entire grain. The expansive nature of Li to diffuse across all GBs is evident, as it proceeds deeper into the material, clearly leaving behind a deteriorated material. After 30,000 h of exposure time, the liquid Li corrodes most GBs in the simulated solid phase. However, it only causes marginal corrosion to the grains on the exposed surface.

Influence of grain size

The grain size plays a governing role in IGC due to the synergistic relationship with GB density within the bulk of the material. As such, the average grain size is altered to observe this dependency. Two additional average grain sizes of 10 and 40 μm are modeled. To isolate the effect of grain

Fig. 4 | Long-term IGC evolution while varying the near-surface grain density. The phase-field variable ϕ in the simulated metallic specimen during a 30,000 h simulation for the three representative microstructures possessing 5, 6, and 7 GBs at the exposed surface.

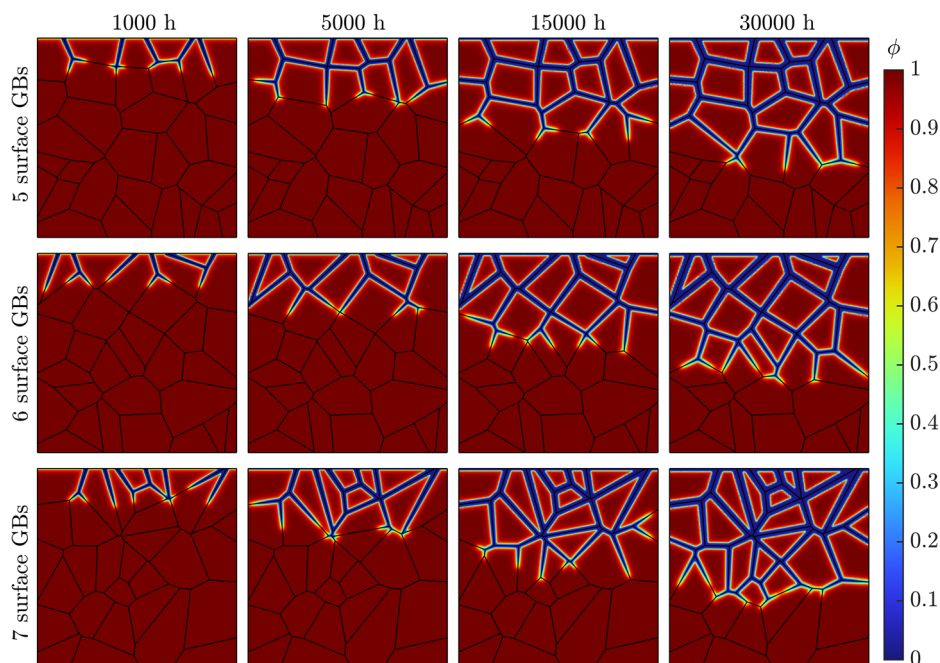
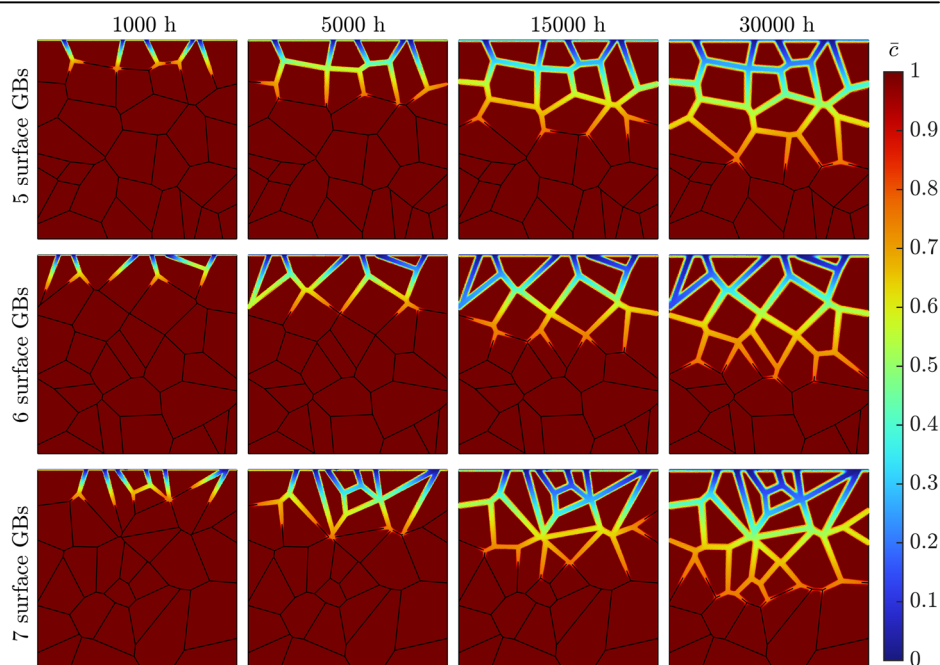


Fig. 5 | Long-term intergranular leaching of Cr while varying the near-surface grain density. The normalized concentration of Cr \bar{c} in the simulated metallic specimen during a 30,000 h simulation for the three representative microstructures possessing 5, 6, and 7 GBs at the exposed surface.



size from near-surface grain density, all three average grain size microstructures should possess the same number of GBs at the exposed surface. Nonetheless, the feasibility of 10 and 40 μm equiaxed microstructures possessing the same number of grains at the exposed surface is unattainable. Therefore, although the near-surface grain density may differ between the three grain sizes (10, 20, and 40 μm), they remain constant within the ten microstructures for each case. As such, the 10 and 40 μm microstructures possess 10 and 2 GBs at the exposed surface. Representative microstructures for all three grain sizes are shown in Fig. 6, while the entire set of microstructures for the 10 and 40 μm microstructures can be seen in Figs. S.4 and S.5 (Supplementary Information). The resultant weight loss and corrosion depth following a 500 h simulation are given in Fig. 7. The SD data at 100, 250, and 500 h exposure time can be seen in Fig. 8.

The weight loss shown in Fig. 7a showcases that the 10 μm average grain size microstructures exhibits the most severe weight loss after 500 h of exposure time. Alternatively, the largest grain size simulated of 40 μm displays the highest corrosion resistance. Unsurprisingly, neither the 10 μm nor the 40 μm microstructures coincide with the experimental data extracted from a 20 μm average grain size F/M specimen. Figure 7b portrays that the average corrosion depth reached by liquid Li is largely independent of the grain size. Although there is little difference between the corrosion depths, there is nonetheless a noticeable pattern in the SDs for each grain size simulated, whereby the 10 μm grain size possesses the smallest SDs and the 40 μm microstructures give rise to the largest SD, more than twice as large as the SDs generated from the 20 μm microstructures, after 500 h (Fig. 8b). The SDs regarding the weight loss show an exceeding variation for

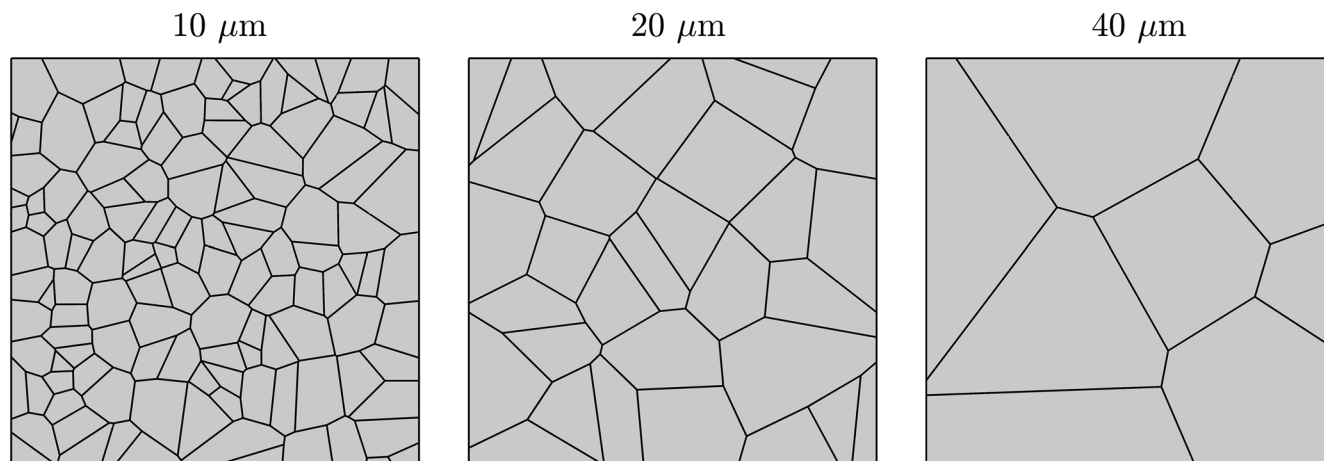


Fig. 6 | Representative microstructures for the three average grain sizes simulated. The GBs present at the exposed surface are 10, 6, and 2 for the 10, 20, and 40 μm microstructures.

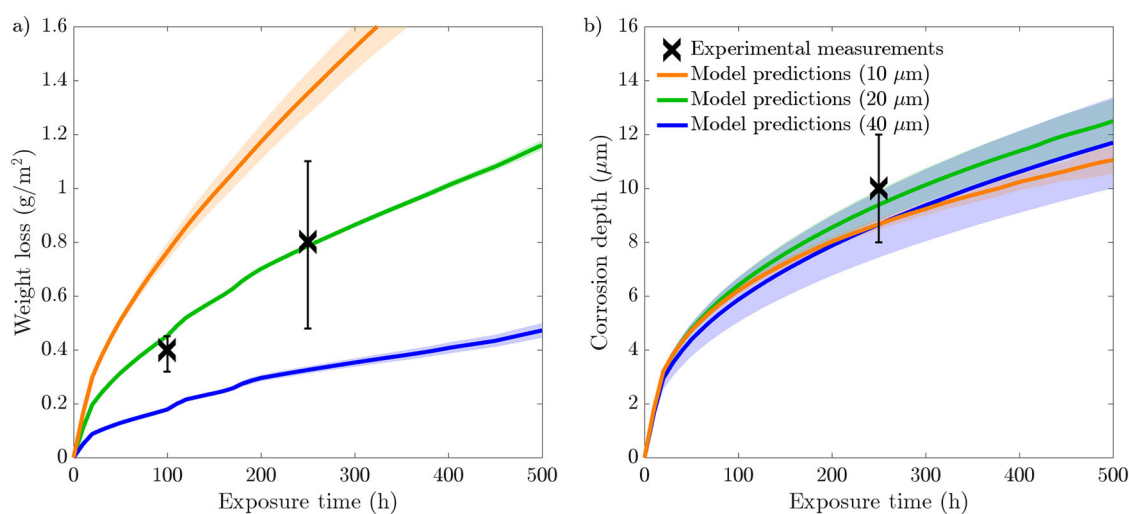


Fig. 7 | Phase-field predictions following a 500 h simulation for 10, 20, and 40 μm average grain size microstructures compared to experimental measurements⁴⁴. Phase-field predictions for **a** weight loss and **b** corrosion depth. The data presented

for each case are taken from an average of ten microstructures where the shaded colored region represents the SD of the ten simulations.

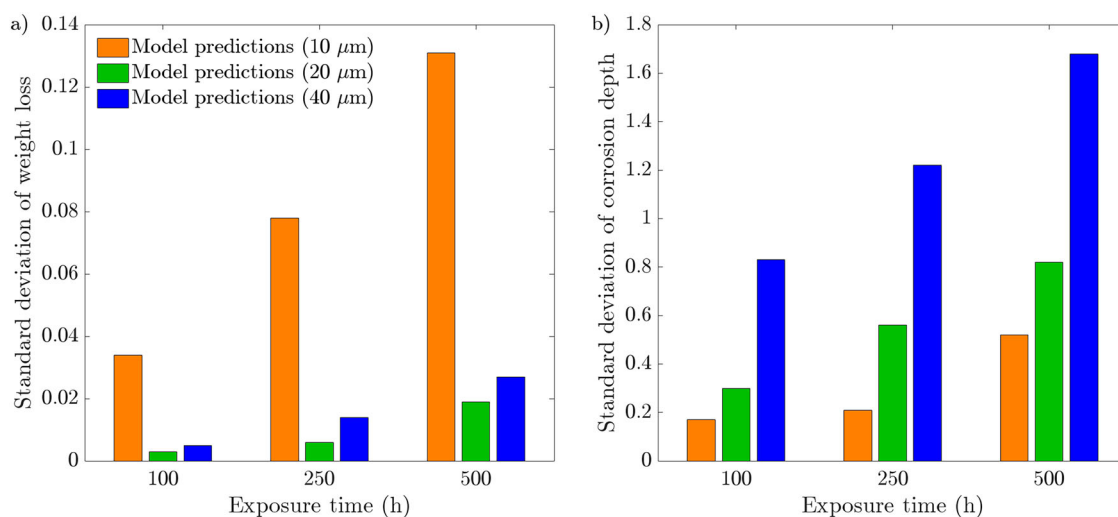


Fig. 8 | Standard deviations at 100, 250, and 500 h intervals for 10, 20, and 40 μm average grain size microstructures. Standard deviations for **a** weight loss and **b** corrosion depth. The data presented for each case are taken from an average of ten microstructures.

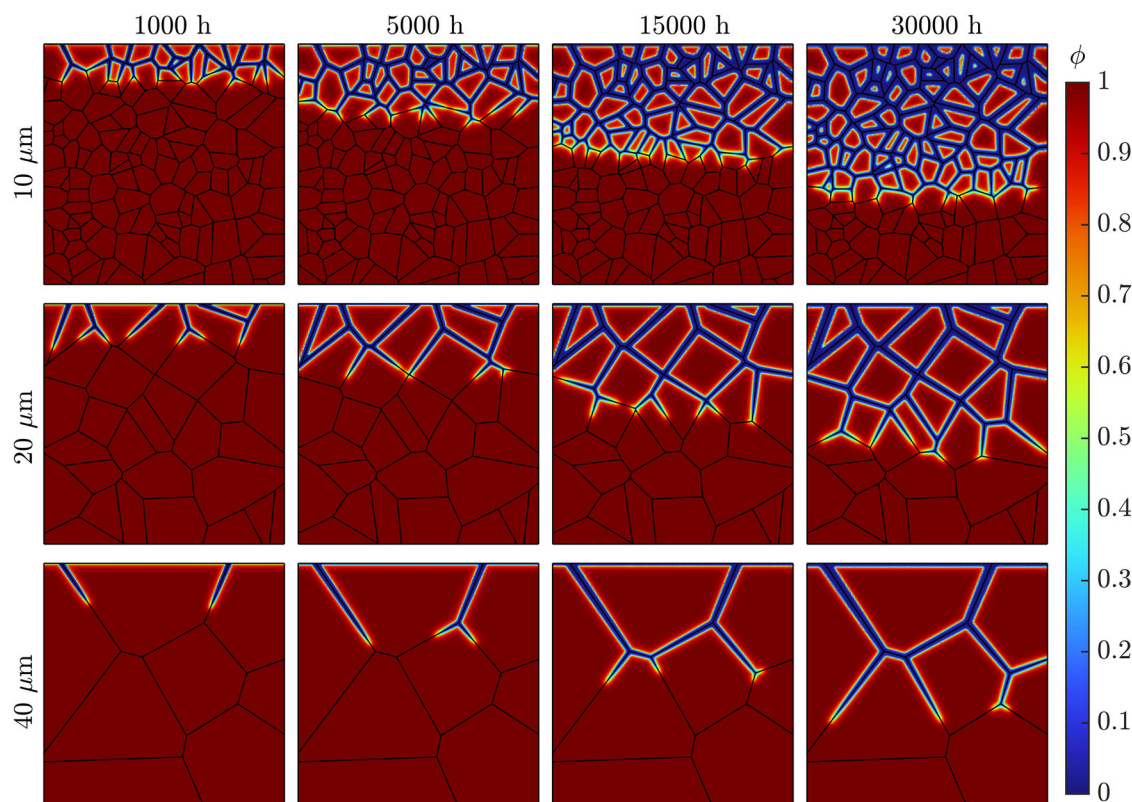


Fig. 9 | Long-term IGC evolution while varying the grain size. The phase-field variable ϕ in the simulated metallic specimen during a 30,000 h simulation for the three representative microstructures with average grain sizes of 10, 20, and 40 μm .

the 10 μm microstructures, whereas the 20 and 40 μm produce similar minute variances.

Figure 9 highlights the IGC evolution across the representative microstructures (Fig. 6) for 30,000 h of exposure time. Analogous to varying the near-surface grain density, the detrimental impact of Li corrosion is apparent, given by the extensive reach during the exposure time. The correlation between the average grain size and severity of corrosion is similarly made clear. The 40 μm microstructure experiences considerably less degradation via the reduced presence of Li within the material. The low density of GBs, resulting in comparatively long GBs with little GB branching, limited the deterioration following exposure to liquid Li. Alternatively, the 10 μm microstructure suffered extreme IGC over the exposure time, established through the vast area of the simulated domain whereby $\phi = 0$. Furthermore, due to the relatively finer grain size, grains are more easily engulfed by Li containing GBs, leaving behind an intricate network of corroded GBs with vastly diminished concentrations of Cr, Fig. 10.

Influence of the thickness of the smeared GB region

As detailed in section "Methods", the computational GB thickness l_p dictates the thickness of the smeared GB region that has increased diffusivity relative to the grains. In addition, implementation of the physical thickness of Cr depletion at the GB, δ_{gb} , circumvents the issue with modeling nanometer-sized features far from their physical dimensions and thus avoids computationally expensive simulations. As such, δ_{gb} is kept constant while l_p is altered to analyze its impact on the corrosion process of the simulated specimen. For this case, the representative microstructures for the 5, 6, and 7 GB microstructures (Fig. 1) were selected. Only a single run is completed for each change in l_p , as running all ten microstructures for each case is not needed to establish a correlation. Figure 11 shows the weight loss and corrosion depth for the three microstructures and the values of l_p chosen: 50, 100, and 200 nm.

For all three types of grain structures with 5, 6, and 7 GBs at the exposed surface, the 50 nm thickness gives rise to the lowest weight loss and 200 nm

thickness results in the most extensive weight loss. That said, the number of GB entry points remains a deciding factor in weight loss. This is most clearly seen for the 7 GB microstructure with 100 nm thickness results in more significant weight loss than for the 5 GB microstructure with 200 nm thickness. This is additionally valid for the 7 GB microstructure with 50 nm thickness when compared against the 5 GB microstructure with 100 nm thickness. On average between all three microstructures simulated, decreasing the computational GB thickness from 100 nm to 50 nm, results in a final weight loss drop of 19.7% whereas when increased from 100 to 200 nm the final weight loss increases by 24.7%. As presented in Fig. 2, there is no obvious relationship between the corrosion depth and the near-surface grain density. Consequentially, varying l_p produces three distinctive groups as opposed to the weight loss data, which is clearly spread. It is clear that the microstructures with 50 nm thickness suffer the greatest corrosion depth, and those with 200 nm thickness have the highest resistance to Li penetration.

Influence of saturation

As stated in section "Model calibration and validation", a concentration sink is implemented to encapsulate the leaching effect of liquid Li in static conditions. This, however, omits the impact of saturation, which hinders and ultimately halts the corrosion process, leading the corrosion data to plateau⁴⁴. To prove the capability of the current model to capture the effect of saturation and to observe whether a concentration sink might influence the corrosion data, a small liquid phase in contact with the solid phase is introduced whereby the concentration sink boundary condition is removed. The incorporation of a liquid phase necessitates a liquid phase diffusivity. That said, as the IGC process depends on the solid-state diffusivity, the value of the liquid phase diffusivity is not of significant importance as long as it is greater than the GB diffusivity. The liquid phase diffusivity of Cr in static liquid Li has been reported to be $2.2 \times 10^{-8} \text{ m}^2/\text{s}$ at 570 $^\circ\text{C}$ ⁴⁵. However, to keep the diffusion coefficient gradient between phases at a manageable difference to avoid unnecessary computational

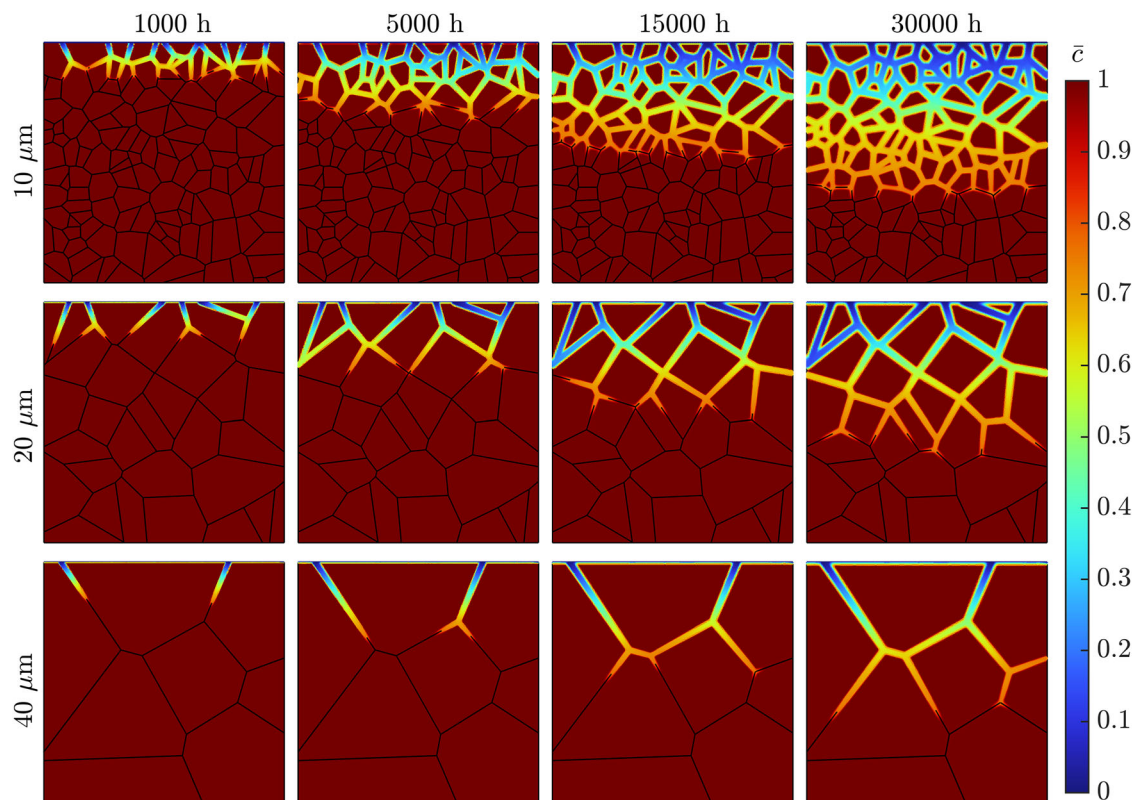


Fig. 10 | Long-term intergranular leaching of Cr while varying the grain size. The normalized concentration of Cr \bar{c} in the simulated metallic specimen during a 30,000 h simulation for the three representative microstructures with average grain sizes of 10, 20, and 40 μm .

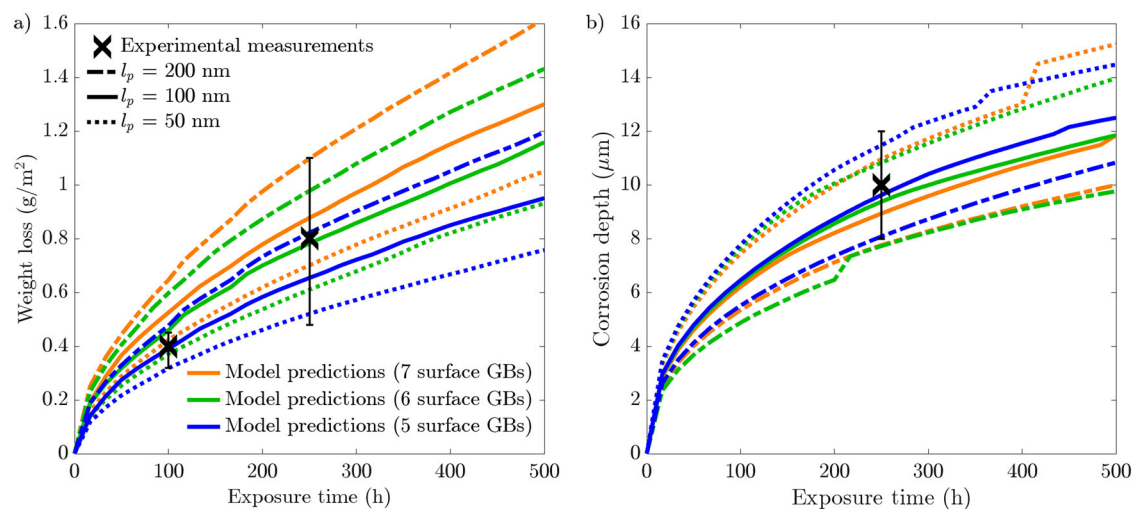


Fig. 11 | Phase-field predictions following a 500 h simulation for 20 μm average grain size geometry with 5, 6, and 7 GBs present at the exposed surface while varying l_p by 50, 100, and 200 nm compared to experimental measurements⁴⁴. Phase-field predictions for **a** weight loss and **b** corrosion depth. The colored lines in

the legend denote the microstructure (i.e., number of near-surface GBs) whereas the black lines of varying line-type illustrate the computational GB thickness l_p . In conjunction they signify the conditions of each dataset.

cost, the liquid phase diffusivity is assigned to be D_{gb} as this will always be greater than D_{gb} .

As the normalized concentration of Cr in the liquid phase (\bar{c}) approaches the normalized equilibrium concentration of the liquid phase ($\bar{c}_{\text{l,eq}}$), the chemical free energy density decreases thereby reducing the chemical driving force of the corrosion process, Eqs. (4) and (5). The diminished chemical driving force decreases the rate of dissolution, thereby producing an asymptotic relationship between \bar{c} and $\bar{c}_{\text{l,eq}}$. As such, herein

saturation of the system is considered met when $\bar{c} \geq 99\% \cdot \bar{c}_{\text{l,eq}}$. It is consequentially found when simulating a 1 μm thick liquid phase in contact with the reference microstructure from section "Model calibration and validation" (i.e., 20 μm average grain size with 6 GBs at the exposed surface) that saturation is achieved after 6000 hours. This is shown in Fig. 12, where the normalized concentration of the liquid phase quickly approaches and eventually reaches the condition of saturation. The thickness of 1 μm is chosen to reach saturation relatively quickly. Consequentially, all

subsequent simulations involving the liquid phase are set with a 6000 h exposure time with a 1 μm thick liquid phase. To survey the influence of the liquid phase, and thus, the effect of saturation on the corrosion process, the liquid phase is introduced to the models described in section "Influence of the liquid phase at the exposed surface" and section "Influence of grain size".

The corrosion data for varying the near-surface grain density can be seen in Fig. 13. As all the microstructures with 5, 6, and 7 GBs are in contact with an identical quantity of liquid phase, the amount of dissolved Cr needed to reach saturation is constant, thereby producing if not identical weight loss profiles resulting in largely consistent final weight loss of 2.22 g/m^2 following 6000 h exposure time, Fig. 13(a). Nonetheless, the weight loss

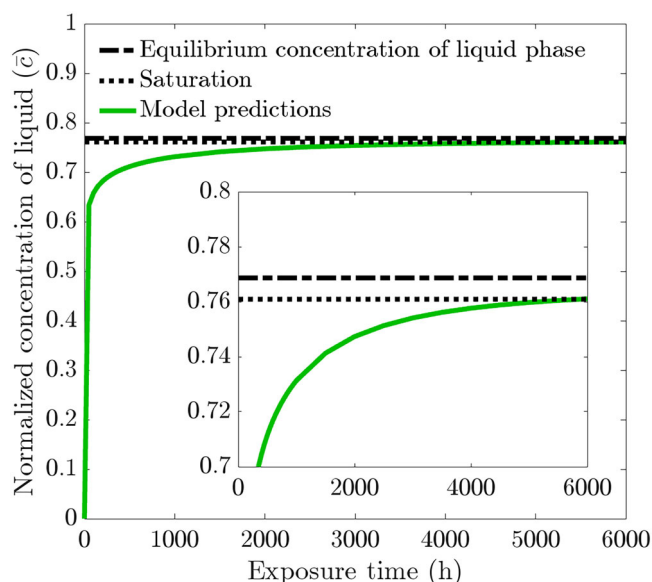


Fig. 12 | Normalized concentration of Cr in the liquid phase as a function of exposure time. With a 1 μm thick liquid phase above a 20 μm average grain size microstructure with 6 GBs, it takes 6000 hours for the system to reach saturation. The data presented here are an average from ten microstructures where the shaded colored region represents the SD of the ten simulations. Note, the consistency across the ten microstructures resulted in a negligible SD. Sub-graph displays a magnified version to clearly highlight the liquid concentration nearing saturation. All subsequent concentration plots possess a range and domain akin to the sub-graph.

experienced by the 7 GB microstructures plateaus before the other two grain structures, indicating the system reached saturation quicker. Therefore, the corrosion process of leaching halted earlier. Alternatively, the 5 GB microstructures take noticeably longer for the weight loss to eventually plateau and terminate. Figure 14(a) reinforces this notion, with the 7 GB microstructures clearly reaching saturation within a shorter exposure time than that of the 6 GB, followed by the 5 GB microstructures. Interestingly, contrary to the results displayed in section "Influence of grain density at the exposed surface" where a concentration sink is implemented, the SDs for the weight loss when saturation is considered are firstly too narrow to have any influential significance and secondly are all consistent across the three types of microstructural conditions simulated. The effect of saturation on the corrosion process is also seen in Fig. 13(b), where corrosion depth eventually plateaus. In this case, there is, although marginal, a clear trend emerging. The 5 GB microstructures produce the deepest depth, followed by the 6 GB, and finally, the 7 GB microstructures give rise to the shallowest corrosion depth. The SDs of the corrosion depths remain in the same order as that found with the concentration sink, where the 5 GB microstructures possess the greatest followed by 6 GB and finally 7 GB microstructures.

Additional analysis is carried out in which the 1 μm thick liquid phase is implemented while varying the average grain size from 10, 20, and 40 μm . Initially, the weight loss data, displayed in Fig. 15(a), shows that the grain size and rate of dissolution are positively correlated. Moreover, the 10 μm microstructures reaches saturation first, indicative of the comparatively early plateau of the weight loss profile. With respect to the 40 μm microstructures, the weight loss profile has yet to plateau, indicating the system did not reach saturation. This is confirmed by Fig. 14(b) whereby the finer grain-sized microstructures bring the system to saturation at the fastest rate. In addition, it is further evident from Fig. 14(b) that the 40 μm microstructures did not reach saturation within the 6000 h exposure time. Interestingly, however, is the progression of the weight loss profile for the 10 μm microstructures, as it peaks around 3000 h, where thereafter begins to dip and drop below the weight loss profile for the 20 μm microstructures. As the same quantity of liquid phase is implemented throughout, the total weight loss experienced strongly resembles the final weight loss when varying the near-surface grain density. Another similarity between Fig. 13(a) and Fig. 15(a) is the negligible SDs. Figure 15(b) displays a clear pattern in the corrosion depth when altering the average grain size of the microstructure. As depicted, the 40 μm microstructures show the deepest corrosion depth, whereas the 10 μm microstructures experiences the shallowest corrosion depth. Furthermore, similar to the weight loss data regarding the 10 μm microstructures, the corrosion depth peaks and subsequently

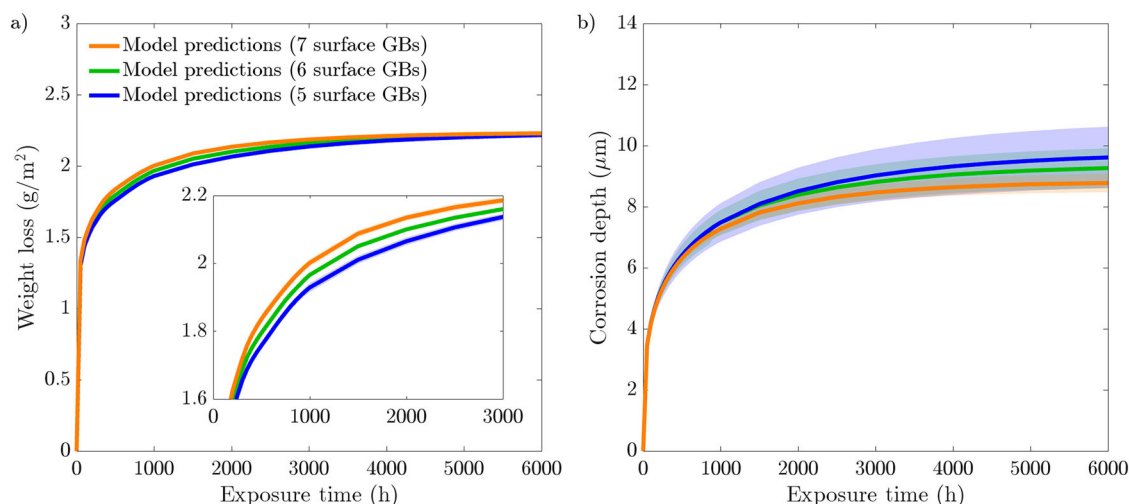


Fig. 13 | Phase-field predictions following a 6000 h simulation for 20 μm average grain size microstructure with 5, 6, and 7 GBs present at the exposed surface with a 1 μm liquid phase in contact with the solid phase. Phase-field predictions for a weight loss and b corrosion depth. The data presented for each case are taken from

an average of ten microstructures each where the shaded colored regions represents the SD of the ten simulations. Sub-graph displays a magnified version to clearly distinguish between the weight loss profiles.

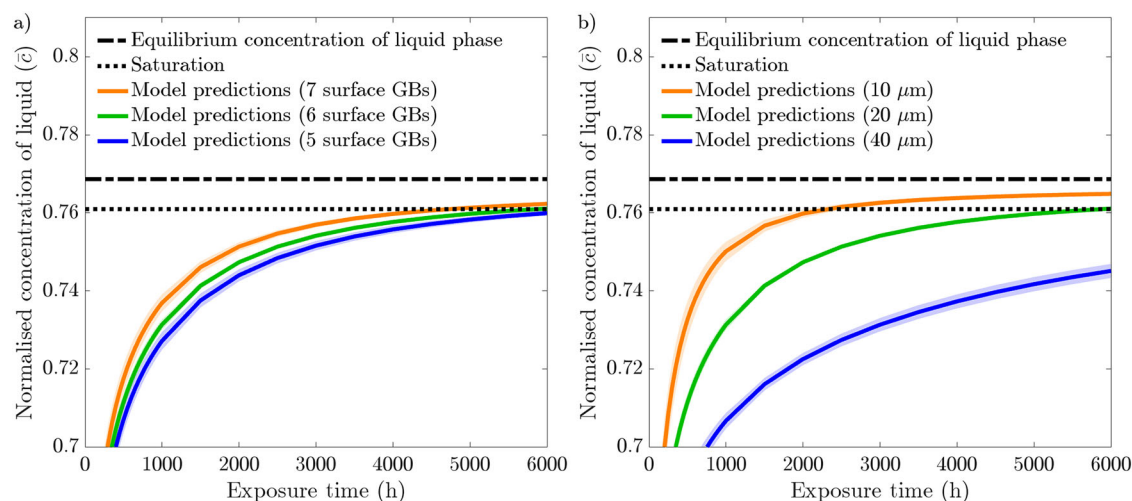


Fig. 14 | Normalized concentration of Cr in the liquid phase as a function of exposure time while varying microstructural properties. Normalized concentration of Cr in the liquid while varying **a** the near-surface grain density for a 20 μm

average grain size microstructure and **b** the average grain size. The data presented for each case are an average of ten microstructures where the shaded colored regions represents the SD of the ten simulations.

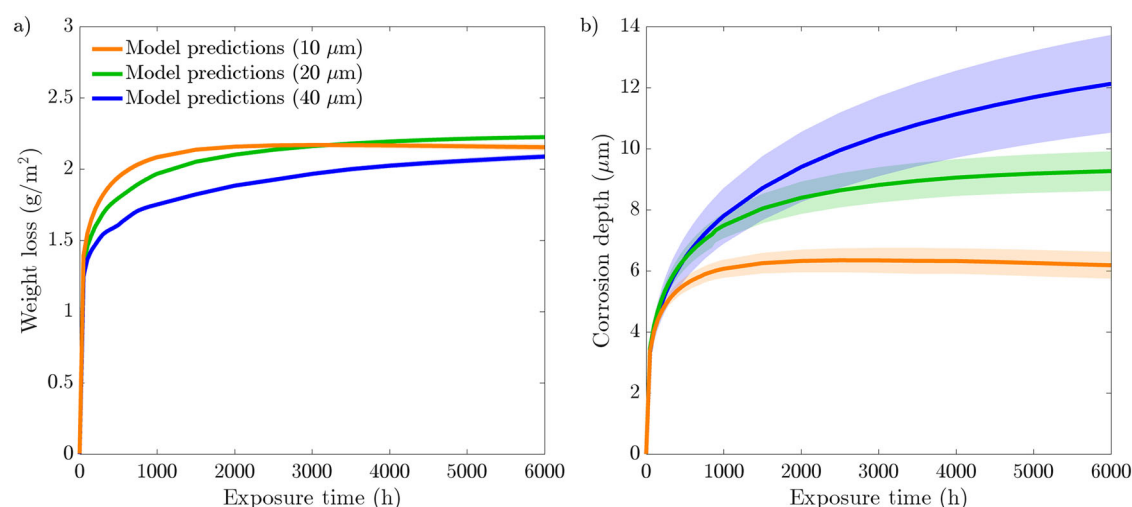


Fig. 15 | Phase-field predictions following a 6000-hour simulation for 10, 20, and 40 μm average grain size with a 1 μm liquid phase in contact with the solid phase. Phase-field predictions for **a** weight loss and **b** corrosion depth. The data presented

for each case is taken from an average of ten microstructures each where the shaded colored regions represents the SD of the ten simulations.

recedes. Analogous to when the concentration sink is implemented, the SDs for the corrosion depth remain in the same order starting at 10, 20, and 40 μm in increasing order.

Discussion

It is clear that the most susceptible microstructures to weight loss possess the greatest number of near-surface grains giving rise to more GB entry points to infiltrate into the material, Fig. 2(a). To emphasize this trend, the inverse projected grain size (G), where G is the ratio of the exposed surface length against the number of near-surface grains, was plotted against the total weight loss (not shown here for brevity). This yielded an R^2 of 0.9973 closely aligning with Bhavé et al.⁴³ reported R^2 of 0.9966, consolidating the significance of GB entry points in IGC. The initial weight loss is dictated by the number of GB entry points, where thereafter, the total length of GBs available to corrode, governed by the grain size, offers a more comprehensive indicator to the degree of dissolution. Reducing the average grain size dramatically increases the density of GBs and thus amplifies the weight loss. Furthermore, the greater variation in the distribution of GBs among the 10 μm microstructures, impacting the amount of accessible GBs, resulted in

high variances in the weight loss, Fig. 8(a), thus behaving more inconsistently relative to the larger grain sizes. The inverse relationship between grain size and IGC susceptibility has been similarly observed experimentally^{46,47}, highlighting the capabilities of the model.

As the corrosion process can continue indefinitely, via the concentration sink, the relationship between corrosion depth and microstructural features is not evident, Figs. 2(b) and 7(b). Nonetheless, it can offer insight into governing traits that dictate the susceptibility of structural materials to corrosion depth. The large variance in corrosion depths for the 40 μm microstructures suggests that penetration depth is highly sensitive to the microstructure when the average grain size is large, Fig. 8(b). The relative orientation of GBs greatly effects the ability of Li to penetrate into the material, whereby the significance of their orientation increases with fewer GB entry points. Furthermore, the degree of GB branching governs the length Li must diffuse before changing its course, placing additional significance on their orientation as it strictly controls the depth Li can reach. Therefore, larger grain sizes produce a greater spread in corrosion depths as opposed to finer grain sizes. This suggest, in light of predictability, that finer grained structural materials are more desirable to optimize consistency in

relation to IGC. That said, a holistic approach need consider the increased susceptibility of IGC as a consequence of the reduced grain size in order to determine the prime microstructure⁴⁸. Likewise when varying the near-surface grain density; the 7 GB microstructures initially possess, albeit marginally, more entry points through which Li penetrates and, therefore, the relative orientation of the GBs has less influence on the depth of corrosion resulting in a lower variance, Fig. 3(b).

Replacement of the concentration sink with the effect of saturation in the corrosion process shifts microstructural influence on the corrosion behavior. Due to the limitless corrosion process brought by the concentration sink, the relationship between the microstructural features (i.e., near-surface grain density and grain size) and weight loss is evident whereas the corrosion depth is independent of any microstructural changes. On the other hand, incorporating a minor quantity of liquid phase, thereby implementing saturation, clearly highlights the synergy between corrosion depth and microstructural features, yet consequentially dampens the correlation with weight loss. It should be noted, the conditions brought by the concentration sink strongly mimic the conditions of a dynamic breeder loop. The thermal gradients of dynamic loops produce detrimental corrosive conditions created by the perpetual dissolution and deposition of material; mass transfer, thus inhibiting saturation^{10,12}. Consequentially, evaluating the corrosion behavior between static (i.e. saturation) and dynamic (i.e. concentration sink) conditions offers insight into the varied compatibility of F/M steels with liquid Li when transitioning from a controlled environment to higher fidelity conditions.

It is apparent that the near-surface grain density dictates the rate of saturation, as it offers more entry points to initiate penetration. Therefore, a greater number of GB entry points yields a faster rate of dissolution thus reaching saturation quicker, Fig. 14(a). This, in turn, controls the corrosion duration before the process is halted, ultimately dictating the depth Li is able to penetrate. The average grain size, via the bulk GB density, has greater influence on the rate of saturation, impacting more heavily the corrosion depth. Moreover, the 40 μm microstructures had yet to reach saturation as seen through the sustained severity of the corrosion depth, Figs. 14(b) and 15(b). Regarding the variance in the corrosion behavior, the introduction of saturation does not affect the order of corrosion depth SDs remaining as $7 < 6 < 5$ GB and $10 < 20 < 40$ μm . Nonetheless, the SDs on weight loss are significantly less prominent when saturation is accounted for. Overall, high density of near-surface grains coupled with small grain size maximizes the rate of saturation, thereby reducing the corrosion duration, and in turn, producing shallower corrosion depths, aligning with experimental reports⁴⁹. It is additionally observed that the corrosion depth and the weight loss for the 10 μm microstructures peak where thereafter it decreases, Fig. 15. As mentioned, near saturation the chemical free energy density decreases considerably, and for the 10 μm microstructures, it becomes smaller than the interfacial free energy term, thus making the latter the dominant term in Eq. (8). Consequentially, the phase-field interface becomes more rigid and thus becomes inapt in simulating complex morphologies causing the IGC pathways to become narrower and shorter during the later stages of exposure, resulting in an apparent diminished weight loss and corrosion depth.

Figures 4 and 9 illustrates the IGC evolution with respect to ϕ , showcasing the diffusive behavior of Li through the material. As the exposure time progresses, near-surface grains are engulfed by corroded GBs, yet the grains remain largely uncorroded. This becomes more apparent as the average grain size decreases. In reality, as corroded GBs surround a grain, they become susceptible to detachment from the bulk matrix, as observed experimentally^{50,51}, producing a surface pebbled morphology. Although the corrosion depth was independent of microstructural features, it is overwhelming apparent that the degree of Li infiltration is strongly correlated to the near-surface and bulk GB density. The greater density of GBs additionally exposes more material to leaching, exacerbating the extent of Cr dissolution in the material, Figs. 5 and 10.

The value of l_p governs the thickness of the Cr depletion region, thus dictating the carbide-rich region whereby Li can penetrate and leach out alloying elements influencing the weight loss. Naturally, a positive

correlation arises between l_p and weight loss, Fig. 11(a). Additionally, attributed to the constant product approach, the value of l_p directly affects the GB diffusivity (D'_{gb}) ultimately altering the kinetics of the reaction. Consequentially, in increasing l_p , Li is unable to penetrate as deep into the material leading to a decreased average corrosion depth, Fig. 11(b). It should be stressed that the width of GB Cr depletion should not impact the kinetics of Li penetration; the observed correlation is purely artificial and attributed to the constant product approach. Nonetheless, the influence on weight loss is valid, which emphasizes the importance of regulating the degree of alloy segregation at the GBs to optimize the resistance of high Cr F/M steels to liquid Li. Moreover, slight kinks, resulting in a sudden jump in corrosion depth, are observed in Fig. 11(b).

Albeit displaying key microstructural features to improve the IGC susceptibility of steel alloys, there remain limitations that dampen the fidelity of the model. To align with the experimental work of Xu et al.⁴⁴, a computationally intensive liquid phase model would be required, necessitating a concentration sink instead. Although a valid assumption prior to saturation, it permits a limitless corrosion process, ultimately resulting in unrealistic behaviors over longer exposure times. Furthermore, the addition of a 1 μm liquid phase required 6000 h for the reference microstructure to saturate, Fig. 12, conflicting with experimental data. The chemical free energy density curvature parameter A is selected based on the accuracy of the phase-field predictions to the experimental data. This proportionality constant should be determined and applied to liquid Li systems to improve the capability of the current framework. The microstructures employed are not fully representative of a tempered martensite microstructure due to the absence of GB angles, thus omitting low-angle GBs (i.e., lath and block boundaries) which should be included to fully capture the microstructural influence of IGC. In addition, the model precluded the nucleation of corrosion products, namely the ternary nitride complex, a prevalent mechanism in liquid Li corrosion with steels⁵². Its formation goes beyond perturbing the chemical potential of the system, thus exacerbating the corrosion process, yet additionally is thought to amplify the kinetics of penetration by fostering a favorable diffusive environment for Li⁵³.

Regarding the long-term performance of the material following exposure to liquid Li, confidence can be placed on the concentration sink model, as this best resembles the continual dissolution conditions of a dynamic breeder blanket. Plus, the long-term behavior of steels with respect to static systems is evidently dependent on the volume of liquid metal used. As detailed, the continual and indefinite corrosion process brought by the concentration sink results in largely identical corrosion depths independent of the grain structure of the specimen. As such, an average corrosion depth from the results displayed in section "Influence of grain density at the exposed surface" and section "Influence of grain size", following 30,000 h, equating to over 3 years of exposure, results in 65.8 μm . This extensive penetration into the material would inevitably cause severe degradation of the mechanical integrity of the material, thereby necessitating routine replacement of the material within this time period. Additionally, the current model assumes the primary degradation mechanism to be intergranular penetration of Li via solubility-driven dissolution. Although this is a governing process in the compatibility between liquid Li and F/M steels, there remain other phenomena not included in the presented model, which would likely exacerbate the penetration rate and thus need to be considered to assess the longevity of these steels. A few notable examples include the impact of non-metallic impurities, thus forming corrosion products, the influence of fluid flow and the effect of dissimilar metallic systems. Compounding these processes in a comprehensive model to accurately evaluate the performance of structural materials with liquid metals is paramount in identifying the ideal candidate for future fusion reactors.

The clear relationship between the microstructure of the specimen and its susceptibility to intergranular penetration, detailed through the model predictions, grants a perspective on the key traits to alter, thereby maximizing the performance of structural alloys in contact with liquid Li. Under an indefinite dissolution process, the grain size should be enlarged, considering desired mechanical properties, to limit the amount of available GBs

to diffuse through and thus corrode. Greater attention should be placed on expanding the size of PAGs as the corresponding GBs, due to their high-angle nature, foster greater density of Cr_{23}C_6 type carbides. Reports have detailed that higher austenitization temperatures over a longer duration facilitate greater growth of austenite grains^{54,55}. Another potential mitigation strategy is to limit the degree of Cr segregation to the GBs either by reducing the carbon content in the steel or by employing high-affinity carbide-forming elements, such as vanadium, niobium, or tantalum^{17,56}. This would additionally diminish the presence of free carbon within the matrix of the steels, reducing the tendency for non-metallic impurity interaction with liquid Li.

To demonstrate the capability of the current model as well as compare the implication in modeling varying dimensions, the results for a 3D simulation following 500 h exposure time are shown in Fig. 16. The geometry and computational conditions of the 3D model mimicked that of the reference 2D model detailed in section "Model calibration and validation", i.e., 100 μm in length and width with a depth of 15 μm . The average grain size of the microstructure was 20 μm with a concentration sink implemented on the upper-most boundary positioned at $z = 15 \mu\text{m}$. The depth of the material was selected to minimize the computational expense and was guided through the final corrosion depth reached following 500 h exposure time with a concentration sink from the 2D models equating to $\sim 12 \mu\text{m}$, Figs. 2 and 7. The evident evolution of the order parameter ϕ along the GBs can be seen in Fig. 16. In accordance to the 2D model, the enhanced corrosion is isolated solely at the boundaries that possesses the heightened

diffusivity, enabling the rapid intergranular extraction of alloying elements. The final weight loss of the 3D microstructure following 500 h exposure time equated in 80.93 g/m^2 , far exceeding the 1.16 g/m^2 experienced for the 2D microstructures detailed in section "Model calibration and validation". It is important to emphasize that in the current formulation, the interface kinetics coefficient L is tailored to 2D microstructures. Therefore, L ought to be derived relative to material properties to generate a more direct linkage between model predictions and experimental data. Bhavé et al.⁴³ similarly reported greater mass loss from the 3D models relative to the 2D models in predicting the IGC behavior of Ni-Cr alloys exposed to molten Li salt. Other similar studies^{40–42,57–59} have been primarily focused on proof-of-concept of their respective formulations rather than analyzing the significance regarding the corrosion data between 2D and 3D simulations. Nonetheless, 2D models have shown to yield representative data, that supports experimental theories, thus formulating our understanding of the microstructural influence on IGC. Future work should consider the role of the flow of the liquid phase, the nucleation of corrosion products from non-metallic impurities, the crystallographic orientation of grains, and GB angle (high and low-angle GBs), in mass transport and IGC of polycrystalline steels. It would additionally be warranted to conduct a parametric study consisting of a larger spectrum of microstructural dimensions (i.e., near-surface grain density and grain size) thus extracting more comprehensive data allowing deeper analysis of their impact on the IGC process.

In conclusion, a numerical framework based on the phase-field method is developed for assessing the IGC of polycrystalline steels with corrosive

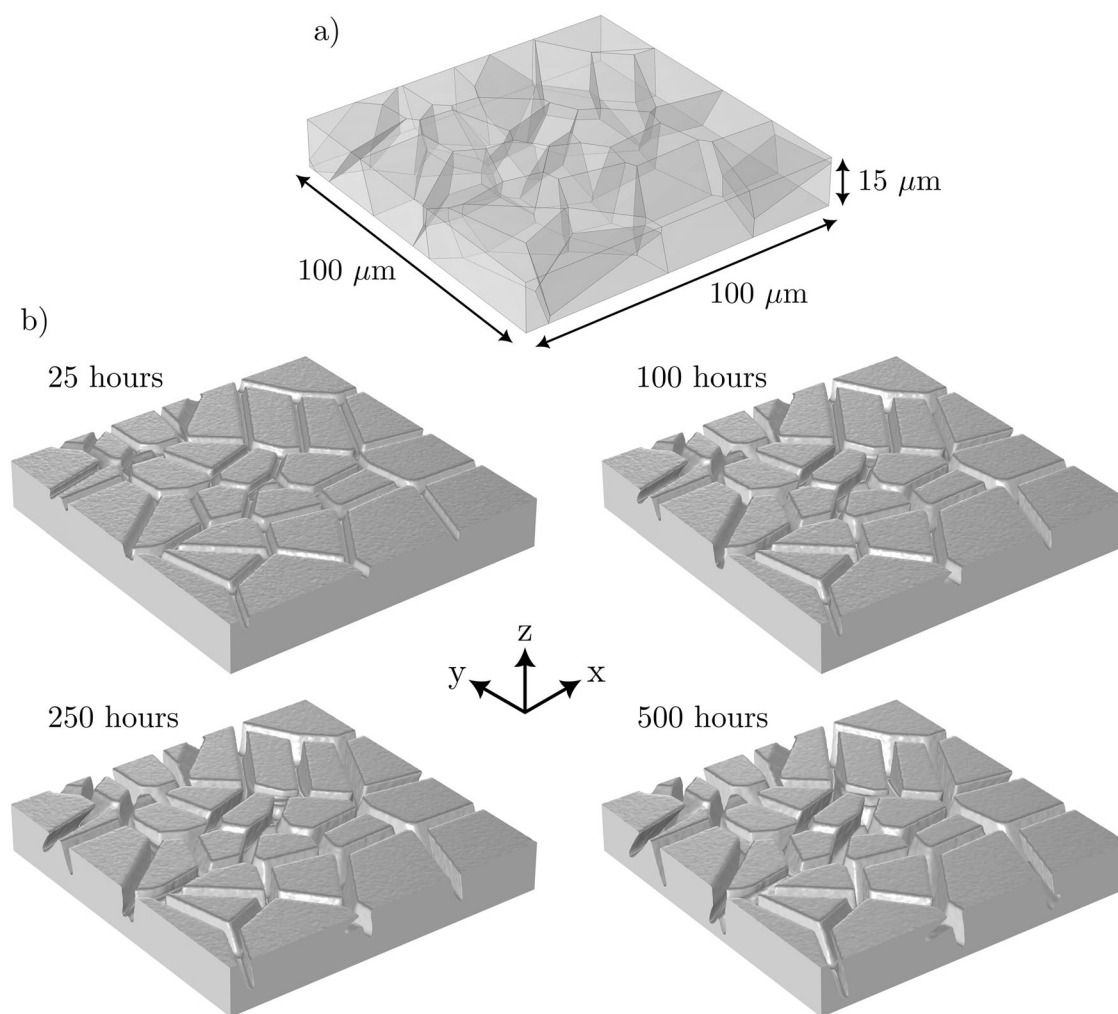


Fig. 16 | 3D simulation of IGC. Depiction of the **a** geometrical dimensions of the 3D model and **b** the intergranular corrosion evolution at 25, 100, 250, and 500 h exposure time. Only the solid phase $\phi \geq 1/2$ is shown for clarity.

media. Herein, the model was applied to capture the leaching effects of liquid Li when in contact with a 9 wt% Cr F/M steel. The key findings can be summarized as follows:

- The governing microstructural features that dominate and ultimately dictate the severity of corrosion are the number of GB entry points, i.e., near-surface grain density. The grain boundary density in the bulk, i.e., grain size, governs the susceptibility to Li corrosion.
- The thickness of Cr depletion along the GBs l_p plays a deciding role in the weight loss of the simulated material. This emphasizes the importance of limiting alloying GB segregation and consequential depletion in these regions, ideally hindering the ability for Li to diffuse intergranularly.
- The effect of saturation is considered and compared against the use of a concentration sink. The former highlights the dependence of the corrosion depth on the microstructural features, whereas the latter amplifies the relationship with weight loss. Although the 10 μm microstructures exhibit the fastest weight loss, this in turn results in the shallowest corrosion depth. With the idea of using grain engineering to maximize the compatibility with Li, it is worth dictating which corrosion behavior is more detrimental to the structural integrity of the alloy.
- The SDs regarding the corrosion depths shed light on the importance of the orientation of the GBs as well as their total length (i.e., GB density) in facilitating the penetration of Li into the material. It is shown that the 40 μm microstructures yield varying corrosion depths as a result.

Methods

Phase-field model of IGC

It is assumed in the current work that the primary degradation mechanism is driven by the bulk diffusion of Cr in the metal phases. These assumptions aligns with^{52,60,61}. The impact of other phases present in the metal (i.e., precipitates and inter-metallic species) and the effect of the Li_2C_2 by-product (Eq. (1)) on the corrosion process is not considered in this study. The following kinematic variables are introduced to characterize the two phases. A continuous phase-field variable $\phi(\mathbf{x}, t)$ is implemented to track each phase and the evolution of the corroding interface. $\phi = 1$ represents the solid phase (i.e., F/M steel), $\phi = 0$ defines the liquid corrosive agent (i.e., liquid Li), and $0 < \phi < 1$ describes the thin diffuse interface separating the opposing phases, Fig. 17. As the composition of Cr in the F/M steels plays arguably the most central role in the corrosion process, modeling the entire composition of the steel is unwarranted. As such, the current model adopts a simplified F/M steel in the form of a simple binary Fe-Cr alloy. The metal phase in the present model is assumed to be Fe-9 wt% Cr steel. It

is further assumed in the present investigation that the material has a uniform composition and is composed of equiaxed grains separated by GBs. The composition of the material and its evolution during corrosion is characterized by the normalized concentration of Cr $\bar{c}(\mathbf{x}, t) = c/c_{\text{solid}}$, where c is the absolute concentration of Cr and c_{solid} the concentration of Cr initially present in the material. Two independent diffusion coefficients between the GB (D_{gb}) and metal grains (D_{mg}) are introduced to enhance the corrosion process along GBs, Fig. 17 whereby the employed values are displayed Table 1. The GB interpolation is achieved via an additional stationary parameter $\eta(\mathbf{x})$, that takes value $\eta = 1$ at the GBs and $\eta = 0$ elsewhere, discussed further below. In the present work, the grains and GBs maintain an isotropic diffusion behavior. The contribution of crystallographic orientation and GB angle (high and low-angle GBs) will be addressed in future work.

For the underlying corrosion mechanism considered, the total free energy functional of the heterogeneous system in Fig. 17 can be expressed as

$$\mathcal{F} = \int_{\Omega} [f^{\text{chem}}(\bar{c}, \phi) + f^{\text{grad}}(\nabla \phi)] d\Omega, \quad (2)$$

where f^{chem} and f^{grad} are the chemical and interfacial free energy densities detailed further below. Ω in the previous expression represents the whole system domain that includes both the corrosive liquid Li environment and the polycrystalline material.

Table 1 | Material and computational parameters employed in the model

Parameter	Value	Unit	Ref
Chemical free energy density curvature parameter A	5×10^9	N/m ²	
Interface kinetics coefficient L	1	m ² /(N · s)	
Concentration in the solid phase c_{solid}	13.4	mol/L	44
Saturated concentration in the liquid phase c_{sat}	10.3	mol/L	20
Interfacial energy Γ	4	N/m	77,78
Computational GB thickness l_p	100	nm	
Physical Cr depletion thickness δ_{gb}	15	nm	79
Interfacial thickness ℓ	4	μm	
Grain boundary diffusivity D_{gb}	1.70×10^{-15}	m ² /s	76
Metal grain diffusivity D_{mg}	5.11×10^{-21}	m ² /s	76

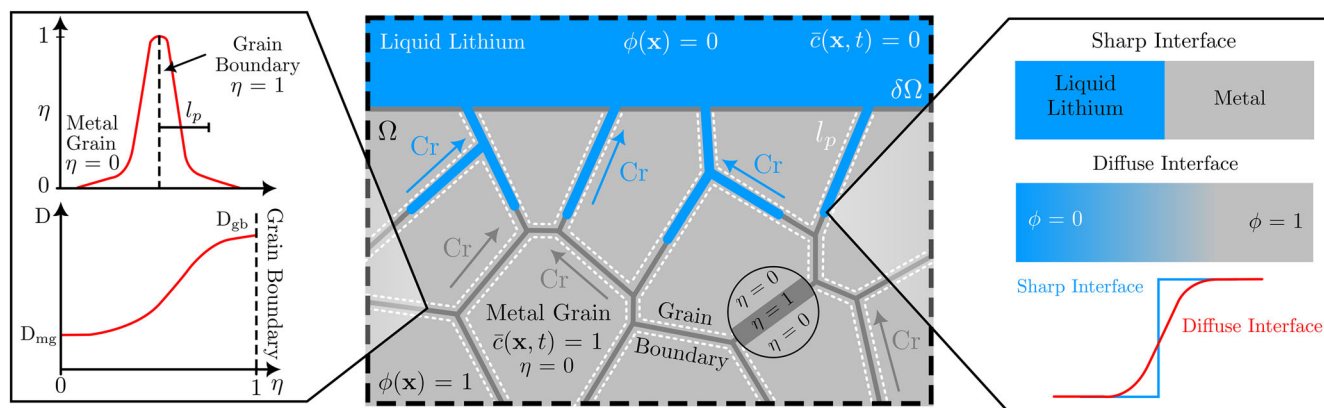
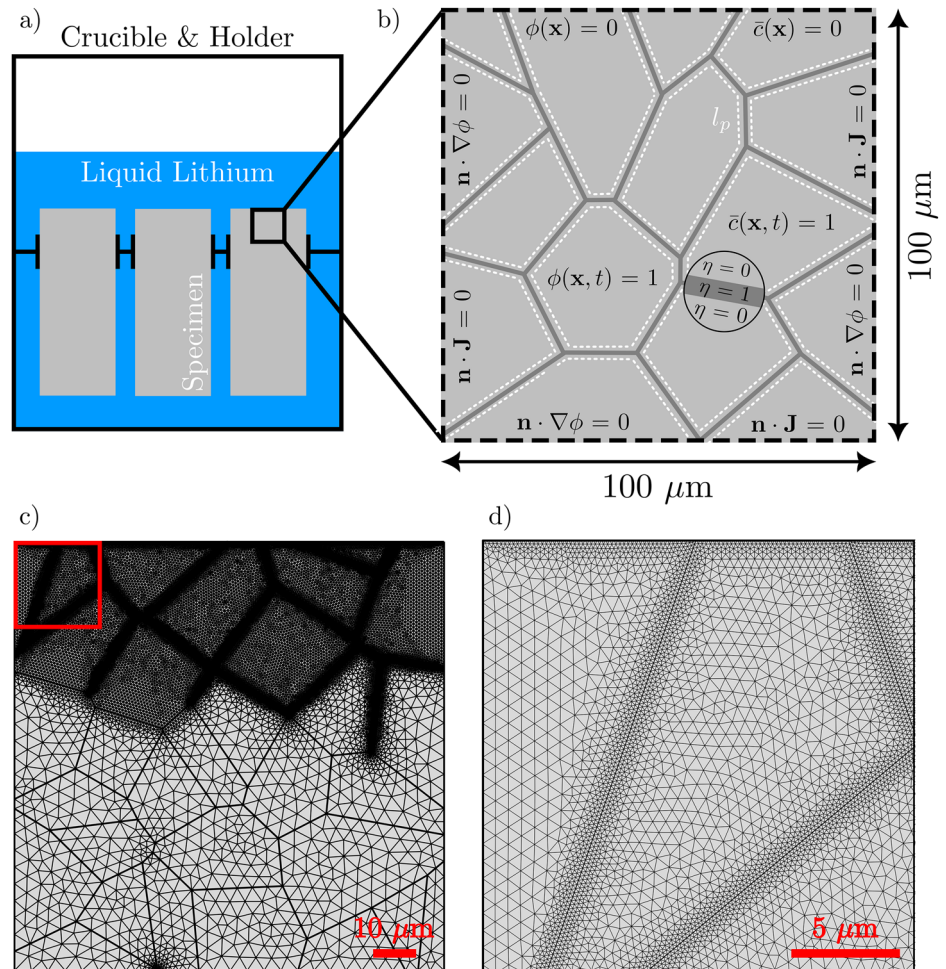


Fig. 17 | Polycrystalline material in contact with a corrosive environment highlighting the diffuse interface between the liquid ($\phi = 0$) and solid ($\phi = 1$) phases. The GBs possess a heightened diffusivity D_{gb} compared to the metal grain D_{mg} via an

additional parameter that differentiates between grain boundary ($\eta = 1$) and metal grain ($\eta = 0$). The corrosion mechanism is based on the bulk diffusion of Cr toward the exposed surface.

Fig. 18 | Computational conditions, domain and meshing. Schematic of the **a** experimental apparatus used by Xu et al.⁴⁴ to expose F/M specimen to static liquid Li, **b** corresponding computational domain consisting of a polycrystalline material with the initial values and boundary conditions, **c** finite element mesh of the whole computational domain, and **d** enlarged area corresponding to the red square in **c** highlighting the finite element size within the grains and along the GBs in the expected area of interface propagation. The exposed surface is the upper most boundary.



The chemical free energy density is expressed as the weighted sum of free energy density from each contributing phase⁶²

$$f^{\text{chem}}(\bar{c}, \phi) = h(\phi)f_s^{\text{chem}}(\bar{c}_s) + (1 - h(\phi))f_l^{\text{chem}}(\bar{c}_l) + \omega g(\phi), \quad (3)$$

where $f_s^{\text{chem}}(\bar{c}_s)$ and $f_l^{\text{chem}}(\bar{c}_l)$ are the chemical free energy densities with respect to the normalized concentrations in the liquid (\bar{c}_l) and solid (\bar{c}_s) phases. $g(\phi) = 16\phi^2(1-\phi)^2$ is the double-well free energy function employed to describe the two equilibrium states for the solid ($\phi = 1$) and the liquid ($\phi = 0$) phases. ω is the constant that determines the height of the energy barrier at $\phi = 1/2$ between the two minima at $\phi = 0$ and $\phi = 1$. $h(\phi) = \phi^3(6\phi^2 - 15\phi + 10)$ is a monotonously increasing interpolation function that interpolates the chemical free energy density between the two phases. The chemical free energy density of each phase can be reasonably approximated by a simple parabolic function⁶³ around equilibrium concentrations with the same free energy density curvature parameter A as³⁰

$$f_s^{\text{chem}}(\bar{c}_s) = \frac{1}{2}A(\bar{c}_s - \bar{c}_{s,\text{eq}})^2 \quad f_l^{\text{chem}}(\bar{c}_l) = \frac{1}{2}A(\bar{c}_l - \bar{c}_{l,\text{eq}})^2, \quad (4)$$

where $\bar{c}_{s,\text{eq}} = c_{\text{solid}}/c_{\text{solid}} = 1$ and $\bar{c}_{l,\text{eq}} = c_{\text{sat}}/c_{\text{solid}}$ are the normalized equilibrium concentrations for the solid and liquid phase. Here, c_{sat} represents the saturation limit of the metal species in the liquid phase. Each material point in the present model is characterized as a mixture of both solid and liquid phases with different compositions, yet the same diffusion chemical potentials⁶⁴. This assumption renders the following expression for

the chemical free energy density $f^{\text{chem}}(\bar{c}, \phi)$ ⁶⁵

$$f^{\text{chem}}(\bar{c}, \phi) = \frac{1}{2}A[\bar{c} - h(\phi)(\bar{c}_{s,\text{eq}} - \bar{c}_{l,\text{eq}}) - \bar{c}_{l,\text{eq}}]^2 + \omega g(\phi). \quad (5)$$

The interfacial free energy density is commonly expressed as

$$f^{\text{grad}}(\nabla\phi) = \frac{1}{2}\kappa|\nabla\phi|^2 \quad (6)$$

where κ is the isotropic gradient energy coefficient. The phase-field parameters ω in Eq. (3) and κ in Eq. (6) are connected to the interfacial energy Γ and the chosen nominal interface thickness ℓ as⁶⁶

$$\kappa = \frac{3}{2}\Gamma\ell \quad \omega = \frac{3\Gamma}{4\ell}. \quad (7)$$

The governing equations for the independent kinematic fields $\phi(\mathbf{x}, t)$ and $\bar{c}(\mathbf{x}, t)$ are derived by minimizing the total energy of the system and conserving the total concentration of Cr composition within the system⁶⁷. The evolution of the non-conserved phase-field parameter ϕ follows the Allen-Cahn equation⁶⁸

$$\frac{\partial\phi}{\partial t} = -L\frac{\delta\mathcal{F}}{\delta\phi} = -L\left(\frac{\partial f^{\text{chem}}}{\partial\phi} - \kappa\nabla^2\phi\right) \quad \text{in } \Omega \quad \kappa\mathbf{n} \cdot \nabla\phi = 0 \quad \text{on } \partial\Omega, \quad (8)$$

where L is the kinetic coefficient that characterizes the interfacial mobility and controls the motion of the solid–liquid interface. The magnitude of this parameter determines the underlying corrosion mechanisms, such as activation-controlled and diffusion-controlled, and regulates the corrosion rate^{29–31,37,69}. The condition for L to capture both mechanisms is given in the following section.

The transport of Cr composition in the system is subject to the conservation law

$$\frac{\partial \bar{c}}{\partial t} = -\nabla \cdot \mathbf{J} \quad \text{in } \Omega \quad \mathbf{J} = -M\nabla \left(\frac{\delta \mathcal{F}}{\delta \bar{c}} \right) \quad \mathbf{n} \cdot \mathbf{J} = 0 \quad \text{on } \partial\Omega, \quad (9)$$

where \mathbf{J} stands for the diffusional flux and M the mobility parameter that characterizes the motion of Cr composition. Here, the mobility parameter is expressed as: $M = D/(\partial^2 f^{\text{chem}}/\partial \bar{c}^2) = D/A^{30}$, where D is the effective diffusion coefficient of Cr composition. After substituting the expression for the mobility parameter into Eq. (9), the diffusional flux is written as

$$\mathbf{J} = -D\nabla \bar{c} - Dh'(\phi)(\bar{c}_{\text{I,eq}} - \bar{c}_{\text{s,eq}})\nabla \phi. \quad (10)$$

The effective diffusion coefficient of Cr composition is interpolated between the grain bulk and GBs as

$$D = D'_{\text{gb}}\eta + (1 - \eta)D_{\text{mg}} \quad D'_{\text{gb}} = \frac{\delta_{\text{gb}}}{l_p}D_{\text{gb}}, \quad (11)$$

where D_{mg} and D_{gb} are the diffusion coefficient of Cr composition in the grain bulk and along GBs, respectively. $D_{\text{gb}} \gg D_{\text{mg}}$ is enforced to enhance the diffusion of Cr composition along GBs. D'_{gb} in the previous equation is the effective diffusion coefficient of Cr composition along GBs defined using the constant product approach⁷⁰. This approach relates the actual diffusion coefficient D_{gb} and the ratio between the physical δ_{gb} and computational thickness l_p of the Cr depletion region along GBs. The expression proportionally alters the GB diffusivity with respect to an experimentally determined GB thickness, which in turn, rectifies the relative contribution of the otherwise unaltered GB diffusivity and additionally decreases the computational expense of simulating nanometer-sized features. The governing equation for the interpolating parameter η is given as⁷¹

$$\nabla \cdot (-l_p^2 \nabla \eta) + \eta = 0 \quad \text{in } \Omega \quad l_p^2 \mathbf{n} \cdot \nabla \eta = 0 \quad \text{on } \partial\Omega \quad \text{and } \eta = 1 \quad \text{on GBs}. \quad (12)$$

GBs are given a value of $\eta = 1$ and smoothly transitions to $\eta \rightarrow 0$ further away from the GBs, Fig. 17. The sensitivity of the evolution of IGC to the computational thickness of the smeared GB region is investigated in section "Influence of the thickness of the smeared GB region". It is assumed in the present formulation that the Cr GB depletion region is given a uniform thickness, neglecting any confinement effects.

The framework developed is implemented into the multi-purpose finite element software package COMSOL multiphysics⁷². The computational domain is discretized using triangular finite elements with second-order Lagrangian interpolation functions. All regions expected to corrode in the metal grains are given a characteristic maximum element size at least five times smaller than the interfacial thickness ℓ to ensure a smooth transition between the metal and corrosive agent. This setting proved sufficient based on previous literature^{30,65,67}. Moreover, as the evolution of the interface is expected to be most prominent at the GBs compared to the metal grain, a maximum element size of $\ell/20$ is applied to all GBs. Finally, to limit the computational cost, the remaining domain of the solid phase is given a maximum element size of ℓ . These conditions are fulfilled in all the simulations. The depictions of the finite element mesh for a representative case study are shown in Fig. 18c, d. Each simulation consists of a two-step study. The governing equation (12) for the interpolating parameter η that defines

the smeared GB thickness is solved in the first step using a steady-state (time-independent) solver. The governing equations (8) and (9) for the evolution of the phase-field parameter ϕ and Cr composition \bar{c} are then solved in the second step using a time-dependent study. An implicit time-stepping method is used for temporal discretization in the time-dependent step. A fully coupled solution algorithm is selected to solve the governing equations. The maximum time step is 2 h. The solver accuracy in each time step is controlled by a relative tolerance of 10^{-4} . The code developed together with example case studies and documentation is available at <https://mechmat.web.ox.ac.uk/codes>.

Model calibration and validation

The model developed is calibrated and validated against experimental data given in⁴⁴ where greater detail regarding the experimental set-up can be found. The steel specimen underwent a normalized and tempered heat treatment resulting in a tempered martensite microstructure with a prior austenitic grain (PAG) size of $20 \mu\text{m}$ ²⁰. The experimental apparatus used by Xu et al. is displayed in Fig. 18. 100 mL of high-purity Li was used, whereby the concentration of nitrogen was estimated to never surpass 100 ppm. Nitrogen has been experimentally reported to exacerbate the corrosion process through chemical reactions producing the stable ternary nitride corrosion product, thereby intensifying the leaching and degradation of structural materials^{52,73}. Nonetheless, following the equilibrium concentration of nitrogen required to form the ternary nitride corrosion complex⁷⁴, the propensity for the corrosion complex to have nucleated and thus contribute to the penetration process was unlikely, consolidating the bulk diffusion mechanism adopted herein. The geometric ratio between the volume of Li to the total surface area of the specimen was $\sim 4 \text{ cm}$. The specimen was exposed to static liquid Li at 600°C for 750 h. Experimental measurements in terms of weight loss and corrosion depth are used to calibrate the model.

The numerical simulation is conducted by considering a 2D computational domain with $100 \mu\text{m}$ in length and height. Only 2D simulations are performed for simplicity, whereby the implications of this assumption are discussed later. The dimensions are selected based on minimizing computational cost while maintaining an adequate region of microstructural features to observe its influence. The computational domain is characterized by a microstructure with an average grain size equal to the PAG size, $20 \mu\text{m}$ from the experiment in⁴⁴, Fig. 18. Solely simulating prior austenitic GBs is a reasonable approximation based on literature that details the extensive corrosion and significant quantity of liquid Li at high-angle GBs following compatibility experiments^{73,75}. Nonetheless, incorporating the entire tempered martensitic constituents (i.e., lath and block boundaries) is important to fully capture the microstructural effects of liquid Li IGC and, as such, this will be investigated in the future. Ten different microstructures are constructed to have a statistically significant sample and generate an average. The ten microstructures used can be viewed in Fig. S.1 (Supplementary Information). The simulation starts by solving for the smeared GB thickness using the governing equation and corresponding boundary conditions in Eq. (12). $\eta = 1$ is enforced on selected GBs that are expected to corrode. Afterward, the resulting set of the governing equations (8) and (9) is solved with accompanying initial and boundary conditions, Fig. 18. The computational domain initially consists solely of the metal phase. Thus, the initial values for the phase-field variable and Cr concentration are set to $\phi = 1$ and $\bar{c} = 1$. The liquid Li phase is represented through a concentration sink implemented by prescribing the Cr concentration to zero. The sink is positioned on the uppermost boundary of the simulated domain. As the simulated solid phase is only exposed from the upper boundary, the other three edges possess zero flux boundary conditions ($\mathbf{n} \cdot \nabla \phi = 0$ and $\mathbf{n} \cdot \mathbf{J} = 0$) for both phase-field variable and Cr concentration. Substituting the liquid phase with a concentration sink does discount the effect of saturation, which ultimately halts the corrosion process in static conditions⁴⁴. Consequently, using a concentration sink to approximate the liquid phase facilitates endless IGC. Yet, it is a justifiable approximation before saturation is reached.

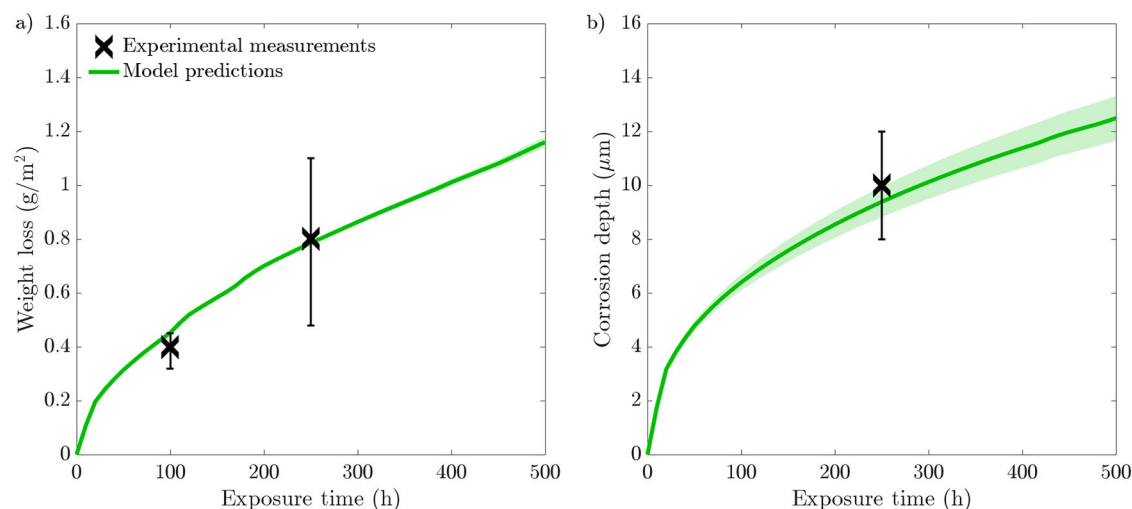


Fig. 19 | Phase-field predictions following a 500 h simulation with a 20 μm average grain size microstructure compared to experimental measurements from Xu et al.⁴⁴. Phase-field predictions for **a weight loss and **b** corrosion depth. The**

data presented is taken from an average of ten microstructures where the shaded colored region represents the SD of the ten simulations.

The material properties and model parameters employed in the simulation are summarized in Table 1. The diffusion coefficients of Cr in the metal grain bulk D_{mg} and along GBs D_{gb} are taken from Čermák et al.⁷⁶. Due to a lack of experimental work, the interfacial energy Γ is obtained based on GB interfacial energies for BCC metals and alloys^{77,78}. A value of $\Gamma = 4 \text{ J/m}^2$ is utilized in the present work. The interfacial thickness ℓ is selected to be significantly smaller than the computational domain and characteristic grain size ($\ell = 4 \text{ }\mu\text{m}$). The phase-field parameters ω (Eq. (5)) and κ (Eq. (6)) are then expressed using ℓ and Γ , as indicated in Eq. (7). The thickness of the Cr-depleted region δ_{gb} is adopted based on experimental work⁷⁹, which found that the thickness varied between 10–15 nm. As such, a conservative approach is taken in the present study, setting $\delta_{\text{gb}} = 15 \text{ nm}$. The computational GB thickness l_p is set to $l_p = 100 \text{ nm}$. The two aforementioned thicknesses; δ_{gb} represents the experimentally determined parameter and l_p signifies the thickness of the simulated GB region, are employed via the constant product approach, to link the artificial microstructure to physical material properties. The chemical free energy density curvature parameter A in Eq. (5) is chosen from similar studies^{29,30,65,67}. Employing the first-principles calculations and the CALPHAD approach can yield a more accurate description of the free energy functional with thermodynamic properties over various compositions and temperatures⁸⁰, which can be fed into the current phase-field framework. The chemical driving force in the present model originates from the difference in Cr composition and the equilibrium values c_{solid} and c_{sat} in each phase, Eq. (5). The former represents the initial known concentration of Cr in a steel specimen before exposure to liquid Li, $c_{\text{solid}} = 13.4 \text{ mol/L}$ ⁴⁴. The latter signifies the equilibrium concentration of Cr in the steel specimen following exposure to liquid Li under static conditions. Due to the extended exposure time tested in the compatibility experiments conducted by Xu et al.⁴⁴, along with the knowledge that chemical equilibrium in static conditions with 100 mL of liquid Li is reached within 250 h^{19,44}, it is warranted to take the post-corrosion test surface concentration of Cr as the equilibrium value, $c_{\text{sat}} = 10.3 \text{ mol/L}$ ²⁰. The interface kinetics coefficient L governs the motion of the metal–liquid interface and, as such, dictates the rate-limiting step of the corrosion process. Comparatively large values give rise to diffusion-controlled corrosion and transitions to activation-controlled as the value decreases²⁹. Dimensional analysis⁶⁷ indicates that L needs to be $L \gg D_{\text{gb}}/(\ell^2\omega)$ for diffusion-controlled and $L \ll D_{\text{gb}}/(\ell^2\omega)$ for activation-controlled regimes. To ensure the corrosion process possesses adequate kinetics to operate under diffusion control, it is given a value of $L = 1 \text{ m}^2/(\text{N} \cdot \text{s})$, which satisfies the previous condition.

The weight loss of the simulated specimen is determined in the simulation as

$$\Delta m = \int_0^{\bar{c}_{\text{Li,eq}}} \bar{c} \cdot c_{\text{solid}} \cdot A_{\text{Cr}} d\Omega, \quad (13)$$

where Δm represents the mass loss in grams and A_{Cr} is the atomic weight of Cr in grams/mole. In accordance with the experimental procedure in evaluating the susceptibility of specimens with liquid Li, the obtained weight loss is normalized with respect to the exposed surface area of the specimen. As such, Eq. (13) is divided by the length of the concentration sink region, 100 μm . The corrosion depth is determined by taking the mean corrosion depth from all advancing corrosion fronts ($\phi < 0.5$) along GBs that are diffusing deeper toward the bulk. Figure 19 illustrates the weight loss and corrosion depth averaged from ten varying microstructures. Figure 19a showcases the strong resemblance between the phase-field predictions and experimental data regarding weight loss. The weight loss predicted by the model passes through the upper relative error at 100 h and matches the experimental data at 250 h with high accuracy. Moreover, the corrosion predictions displayed in Fig. 19b similarly shows a high correlation to the experimental data, resulting in a corrosion depth of 9.4 μm after 250 h. After 500 h, the model predicted an average weight loss of 1.16 g/m² where the liquid Li reached an average depth of 12.5 μm . The logarithmically varying profile for the weight loss and corrosion depth signifies that the corrosion process is in the diffusion-controlled region, further aligning with the literature and proving that the phase-field mobility parameter L is adequately selected. The close comparison between the phase-field predictions and experimental measurements⁴⁴ showcases the capabilities of the current model to simulate IGC. Following model calibration and validation, microstructural and GB properties are altered to observe their dependence on the corrosion resistance of the simulated F/M specimen to static liquid Li in section "Results". The data are compared against the reference geometry described in this section.

Data availability

The relevant data are available from the corresponding authors upon reasonable request.

Code availability

The code developed together with example case studies and documentation is available at <https://mechmat.web.ox.ac.uk/codes>.

Received: 6 February 2025; Accepted: 29 May 2025;

Published online: 10 June 2025

References

1. Smith, D. Blanket materials for DT fusion reactors. *J. Nucl. Mater.* **103**, 19–29 (1981).
2. Shanliang, Z. & Yican, W. Neutronic comparison of tritium-breeding performance of candidate tritium-breeding materials. *Plasma Sci. Technol.* **5**, 1995–2000 (2003).
3. Malang, S. & Mattas, R. Comparison of lithium and the eutectic lead–lithium alloy, two candidate liquid metal breeder materials for self-cooled blankets. *Fusion Eng. Des.* **27**, 399–406 (1995).
4. Kirillov, I., Shatalov, G. & Strebkov, Y. RF TBMs for ITER tests. *Fusion Eng. Des.* **81**, 425–432 (2006).
5. Bloom, E. E. The challenge of developing structural materials for fusion power systems. *J. Nucl. Mater.* **258–263**, 7–17 (1998).
6. Giancarli, L. et al. Breeding blanket modules testing in ITER: an international program on the way to DEMO. *Fusion Eng. Des.* **81**, 393–405 (2006).
7. Smith, D., Billone, M., Majumdar, S., Mattas, R. & Sze, D.-K. Materials integration issues for high performance fusion power systems. *J. Nucl. Mater.* **258–263**, 65–73 (1998).
8. Giancarli, L. M. et al. Overview of recent ITER TBM program activities. *Fusion Eng. Des.* **158**, 111674 (2020).
9. Klueh, R. L. Elevated temperature ferritic and martensitic steels and their application to future nuclear reactors. *Int. Mater. Rev.* **50**, 287–310 (2005).
10. Chopra, O. K. & Tortorelli, P. F. Compatibility of materials for use in liquid-metal blankets of fusion reactors. *J. Nucl. Mater.* **123**, 1201–1212 (1984).
11. Tortorelli, P. F. & DeVan, J. H. Oak Ridge National Lab (ed.) Liquid metal corrosion considerations in alloy development. (Oak Ridge National Lab., 1984).
12. Tortorelli, P. F. Corrosion of ferritic steels by molten lithium: influence of competing thermal gradient mass transfer and surface product reactions. *J. Nucl. Mater.* **155–157**, 722–727 (1988).
13. Lyublinski, I., Evtikhin, V., Pankratov, V. & Krasin, V. Numerical and experimental determination of metallic solubilities in liquid lithium, lithium-containing nonmetallic impurities, lead and lead–lithium eutectic. *J. Nucl. Mater.* **224**, 288–292 (1995).
14. Chopra, O. K. & Smith, D. L. Compatibility of ferritic steels in forced circulation lithium and Pb–17Li systems. *J. Nucl. Mater.* **155–157**, 715–721 (1988).
15. Tortorelli, P. & Chopra, O. Corrosion and compatibility considerations of liquid metals for fusion reactor applications. *J. Nucl. Mater.* **103**, 621–632 (1981).
16. Ruedl, E., Coen, V., Sasaki, T. & Kolbe, H. Intergranular lithium penetration of low-Ni, Cr–Mn austenitic stainless steels. *J. Nucl. Mater.* **110**, 28–36 (1982).
17. Bell, G. E. & Abdou, M. A. The role of carbides in the corrosion behavior of Fe–12Cr–1MoVW steel in liquid lithium. *Fusion Technol.* **15**, 315–320 (1989).
18. Hosaka, T., Kondo, M., Sato, S., Ando, M. & Nozawa, T. Chemical compatibility of F82H and 316L in liquid metal heat transfer mediums Li, Na and NaK. *J. Nucl. Mater.* **561**, 153546 (2022).
19. Xu, Q., Nagasaka, T. & Muroga, T. Compatibility of low activation ferritic steels with liquid lithium. *Fusion Sci. Technol.* **52**, 609–612 (2007).
20. Tsisar, V., Kondo, M., Muroga, T., Nagasaka, T. & Yeliseyeva, O. Structural and compositional transformations in the near-surface layers of Fe–Cr based steels exposed to lithium – effect of alloying and corrosion-assisted substructure coarsening. *Corros. Sci.* **53**, 441–447 (2011).
21. Zhang, D. et al. Study on corrosion behavior of China low activation ferritic/martensitic steel in static liquid lithium. *Nucl. Mater. Energy* **38**, 101594 (2024).
22. Sarkar, S., Warner, J. E. & Aquino, W. A numerical framework for the modeling of corrosive dissolution. *Corros. Sci.* **65**, 502–511 (2012).
23. Sun, W., Wang, L., Wu, T. & Liu, G. An arbitrary Lagrangian–Eulerian model for modelling the time-dependent evolution of crevice corrosion. *Corros. Sci.* **78**, 233–243 (2014).
24. Jafarzadeh, S., Chen, Z., Zhao, J. & Bobaru, F. Pitting, lacy covers, and pit merger in stainless steel: 3D peridynamic models. *Corros. Sci.* **150**, 17–31 (2019).
25. Chen, Z. & Bobaru, F. Peridynamic modeling of pitting corrosion damage. *J. Mech. Phys. Solids* **78**, 352–381 (2015).
26. Gong, K., Wu, M., Liu, X. & Liu, G. Nucleation and propagation of stress corrosion cracks: modeling by cellular automata and finite element analysis. *Mater. Today Commun.* **33**, 104886 (2022).
27. Fatoba, O., Leiva-Garcia, R., Lishchuk, S., Larrosa, N. & Akid, R. Simulation of stress-assisted localised corrosion using a cellular automaton finite element approach. *Corros. Sci.* **137**, 83–97 (2018).
28. Martínez-Pañeda, E. Phase-field simulations opening new horizons in corrosion research. *MRS Bull.* **49**, 603–612 (2024).
29. Cui, C., Ma, R. & Martínez-Pañeda, E. Electro-chemo-mechanical phase field modeling of localized corrosion: theory and COMSOL implementation. *Eng. Comput.* **39**, 3877–3894 (2023).
30. Makuch, M., Kovacevic, S., Wenman, M. R. & Martínez-Pañeda, E. A microstructure-sensitive electro-chemo-mechanical phase-field model of pitting and stress corrosion cracking. *Corros. Sci.* **232**, 112031 (2024).
31. Ansari, T. Q., Luo, J.-L. & Shi, S.-Q. Modeling the effect of insoluble corrosion products on pitting corrosion kinetics of metals. *npj Mater. Degrad.* **3**, 28 (2019).
32. Lin, C. & Ruan, H. Phase-field modeling of mechano–chemical-coupled stress-corrosion cracking. *Electrochim. Acta* **395**, 139196 (2021).
33. Tantratian, K., Yan, H. & Chen, L. Predicting pitting corrosion behavior in additive manufacturing: electro-chemo-mechanical phase-field model. *Comput. Mater. Sci.* **213**, 111640 (2022).
34. Brewick, P. T. Simulating pitting corrosion in AM 316L microstructures through phase field methods and computational modeling. *J. Electrochem. Soc.* **169**, 011503 (2022).
35. Amador, J., Vega, J., García-Lecina, E. & Varas, F. Quantitative phase-field model to simulate low carbon steel aqueous corrosion phenomena. *Corros. Sci.* **232**, 112045 (2024).
36. Chadwick, A. F., Stewart, J. A., Enrique, R. A., Du, S. & Thornton, K. Numerical modeling of localized corrosion using phase-field and smoothed boundary methods. *J. Electrochem. Soc.* **165**, C633–C646 (2018).
37. Kandekar, C., Ravikumar, A., Höche, D. & Weber, W. E. Mastering the complex time-scale interaction during Stress Corrosion Cracking phenomena through an advanced coupling scheme. *Comput. Methods Appl. Mech. Eng.* **428**, 117101 (2024).
38. Li, B., Xing, H. & Jing, H. New diffusive interface model for pitting corrosion. *npj Mater. Degrad.* **7**, 84 (2023).
39. Jafarzadeh, S., Chen, Z. & Bobaru, F. Peridynamic modeling of intergranular corrosion damage. *J. Electrochem. Soc.* **165**, C362–C374 (2018).
40. Guiso, S., di Caprio, D., de Lamare, J. & Gwinner, B. Intergranular corrosion: comparison between experiments and cellular automata. *Corros. Sci.* **177**, 108953 (2020).
41. Guiso, S. et al. Intergranular corrosion in evolving media: Experiment and modeling by cellular automata. *Corros. Sci.* **205**, 110457 (2022).
42. Ansari, T. Q., Luo, J.-L. & Shi, S.-Q. Multi-phase-field model of intergranular corrosion kinetics in sensitized metallic materials. *J. Electrochem. Soc.* **167**, 061508 (2020).
43. Vivek Bhave, C., Zheng, G., Sridharan, K., Schwen, D. & Tonks, M. R. An electrochemical mesoscale tool for modeling the corrosion of structural alloys by molten salt. *J. Nucl. Mater.* **574**, 154147 (2023).
44. Xu, Q. et al. Corrosion characteristics of low activation ferritic steel, JLF-1, in liquid lithium in static and thermal convection conditions. *Fusion Eng. Des.* **83**, 1477–1483 (2008).

45. Griaznov, G. M., Evtikhin, V. A., Zaviatski, L. P., Kosuhin, A. Y. & Lyublinski, I. E. Interaction of structural materials with liquid metals under the isothermal conditions. *Material science of liquid metal systems of thermonuclear reactors*, Energoatomizdat 32–142 (1989).
46. Tortorelli, P. F. & DeVan, J. H. Mass transfer behavior of a modified austenitic stainless steel in lithium. *J. Nucl. Mater.* **123**, 1258–1263 (1984).
47. Li, Y., Abe, H., Nagasaka, T., Muroga, T. & Kondo, M. Corrosion behavior of 9Cr-ODS steel in stagnant liquid lithium and lead–lithium at 873K. *J. Nucl. Mater.* **443**, 200–206 (2013).
48. Hariharan, K. & Virtanen, S. Microstructure engineering for corrosion resistance in structural alloy design. *npj Mater. Degrad.* **8**, 115 (2024).
49. DiStefano, J. Corrosion of refractory metals by lithium. Ph.D. thesis (Oak Ridge National Laboratory, 1964).
50. Kondo, M., Muroga, T., Nagasaka, T., Tsisar, V. & Yeliseyeva, O. Erosion–corrosion of RAFM JLF-1 steel in lithium flow induced by impeller. *J. Plasma Fusion Res.* **9**, 294–299 (2010).
51. Kondo, M. et al. Flow accelerated corrosion and erosion–corrosion of RAFM steel in liquid breeders. *Fusion Eng. Des.* **86**, 2500–2503 (2011).
52. Tsisar, V. et al. Effect of nitrogen on the corrosion behavior of RAFM JLF-1 steel in lithium. *J. Nucl. Mater.* **417**, 1205–1209 (2011).
53. Beskorovaynyi, N. M. & Ioltuhovski, A. G. Mechanisms of corrosion processes under the contact of structural materials with liquid lithium. Structural materials and liquid metal heat-transfers, Energoatomizdat, Moscow 59–89 (1983).
54. Lee, S. J. & Lee, Y.-K. Effect of austenite grain size on martensitic transformation of a low alloy steel. *Mater. Sci. Forum* **475–479**, 3169–3172 (2005).
55. Souza, S. d. S. d., Moreira, P. S. & Faria, G. L. d. Austenitizing temperature and cooling rate effects on the martensitic transformation in a microalloyed-steel. *Mater. Res.* **23**, 0570 (2020).
56. Tortorelli, P. F., Devan, J. H. & Yonco, R. M. Compatibility of Fe–Cr–Mo alloys with static lithium. *J. Mater. Energy Syst.* **2**, 5–15 (1981).
57. Zhang, J., Chen, Z. H. & Dong, C. F. Simulating intergranular stress corrosion cracking in AZ31 using three-dimensional cohesive elements for grain structure. *J. Mater. Eng. Perform.* **24**, 4908–4918 (2015).
58. Nguyen, T.-T., Réthoré, J., Yvonnet, J. & Baietto, M.-C. Multi-phase-field modeling of anisotropic crack propagation for polycrystalline materials. *Comput. Mech.* **60**, 289–314 (2017).
59. Simonovski, I. & Cizelj, L. Computational multiscale modeling of intergranular cracking. *J. Nucl. Mater.* **414**, 243–250 (2011).
60. Reeves, J. A., Olson, D. L. & Bradley, W. L. Grain boundary penetration kinetics of nitrated type 304L stainless steel. *Nucl. Technol.* **30**, 385–389 (1976).
61. Patterson, R., Schlager, R. & Olson, D. Lithium grain-boundary penetration of 304L stainless steel. *J. Nucl. Mater.* **57**, 312–316 (1975).
62. Wheeler, A. A., Boettinger, W. J. & McFadden, G. B. Phase-field model for isothermal phase transitions in binary alloys. *Phys. Rev. A* **45**, 7424–7439 (1992).
63. Hu, S., Murray, J., Weiland, H., Liu, Z. & Chen, L. Thermodynamic description and growth kinetics of stoichiometric precipitates in the phase-field approach. *Calphad* **31**, 303–312 (2007).
64. Kim, S. G., Kim, W. T. & Suzuki, T. Phase-field model for binary alloys. *Phys. Rev. E* **60**, 7186–7197 (1999).
65. Makuch, M., Kovacevic, S., Wenman, M. R. & Martínez-Pañeda, E. A nonlinear phase-field model of corrosion with charging kinetics of electric double layer. *Model. Simul. Mater. Sci. Eng.* **32**, 075012 (2024).
66. Kovacevic, S., Pan, R., Sekulic, D. & Mesarovic, S. Interfacial energy as the driving force for diffusion bonding of ceramics. *Acta Materialia* **186**, 405–414 (2020).
67. Kovacevic, S., Ali, W., Martínez-Pañeda, E. & LLorca, J. Phase-field modeling of pitting and mechanically-assisted corrosion of Mg alloys for biomedical applications. *Acta Biomaterialia* **164**, 641–658 (2023).
68. Allen, S. M. & Cahn, J. W. A microscopic theory for antiphase boundary motion and its application to antiphase domain coarsening. *Acta Metall.* **27**, 1085–1095 (1979).
69. Mai, W. & Soghrati, S. New phase field model for simulating galvanic and pitting corrosion processes. *Electrochim. Acta* **260**, 290–304 (2018).
70. Simon, P.-C., Aagesen, L. K., Jiang, C., Jiang, W. & Ke, J.-H. Mechanistic calculation of the effective silver diffusion coefficient in polycrystalline silicon carbide: application to silver release in AGR-1 TRISO particles. *J. Nucl. Mater.* **563**, 153669 (2022).
71. Nguyen, T., Yvonnet, J., Zhu, Q.-Z., Bornert, M. & Chateau, C. A phase-field method for computational modeling of interfacial damage interacting with crack propagation in realistic microstructures obtained by microtomography. *Comput. Methods Appl. Mech. Eng.* **312**, 567–595 (2016).
72. COMSOL Multiphysics v. 6.0. <https://www.comsol.com>. COMSOL AB, Stockholm, Sweden.
73. Coen, V. & Fenici, P. Compatibility of structural materials with liquid breeders – a review of recent work carried out at JRC, Ispra. *Nucl. Eng. Des. Fusion* **1**, 215–229 (1984).
74. Knaster, J. & Favuzza, P. Assessment of corrosion phenomena in liquid lithium at 873 K. A Li(d,n) neutron source as case study. *Fusion Eng. Des.* **118**, 135–141 (2017).
75. Ruedl, E. & Sasaki, T. Effect of lithium on grain-boundary precipitation in a Cr–Mn austenitic steel. *J. Nucl. Mater.* **116**, 112–122 (1983).
76. Čermák, J., Ružicková, J. & Pokorná, A. Low-temperature tracer diffusion of chromium in Fe–Cr ferritic alloys. *Scr. Materialia* **35**, 411–416 (1996).
77. Li, C., Lu, S., Divinski, S. & Vitos, L. Theoretical and experimental grain boundary energies in body-centered cubic metals. *Acta Materialia* **255**, 119074 (2023).
78. Scheiber, D., Pippan, R., Puschnig, P. & Romaner, L. Ab initio calculations of grain boundaries in bcc metals. *Model. Simul. Mater. Sci. Eng.* **24**, 035013 (2016).
79. Nakamichi, H., Sato, K., Miyata, Y., Kimura, M. & Masamura, K. Quantitative analysis of Cr-depleted zone morphology in low carbon martensitic stainless steel using FE-(S)TEM. *Corros. Sci.* **50**, 309–315 (2008).
80. Kumar Thakur, A., Kovacevic, S., Manga, V. R., Deymier, P. A. & Muralidharan, K. A first-principles and CALPHAD-assisted phase-field model for microstructure evolution: application to Mo–V binary alloy systems. *Mater. Des.* **235**, 112443 (2023).

Acknowledgements

This work is supported by the EPSRC Center for Doctoral Training in Nuclear Energy Futures and the agreement between UKAEA and Imperial College London (EP/S023844/1). D.N.-M. work has been carried out within the framework of the EUROfusion Consortium, funded by the European Union via the Euratom Research and Training Program (101052200 – EUROfusion). The work at UKAEA was partially supported by the Broader Approach Phase II agreement under the PA of IFERC2-T2PA02. Views and opinions expressed are, however, those of the author(s) only and do not necessarily reflect those of the European Union or the European Commission. Neither the European Union nor the European Commission can be held responsible for them. D.N.-M. and J.L. also acknowledge funding by the EPSRC Energy Program (EP/W006839/1). S.K. and E.M.-P. acknowledge financial support from UKRI's Future Leaders Fellowship program (Grant MR/V024124/1).

Author contributions

A.L.: Writing—original draft, visualization, validation, software, methodology, investigation, formal analysis, data curation, and conceptualization. S.K.: Writing—review & editing, supervision, software, methodology, investigation, formal analysis, and conceptualization. D.N.-M.: Writing—review & editing, supervision, project administration, funding acquisition, and conceptualization. J.L.: Writing—review & editing, supervision, project administration, funding acquisition, and conceptualization. E.M.-P.: Writing—review & editing,

supervision, software, resources, project administration, methodology, funding acquisition, and conceptualization. M.W.: Writing—review & editing, supervision, project administration, funding acquisition, and conceptualization. All authors have read and approved the manuscript.

Competing interests

The authors declare no competing interests.

Additional information

Supplementary information The online version contains supplementary material available at <https://doi.org/10.1038/s41529-025-00616-4>.

Correspondence and requests for materials should be addressed to Emilio Martínez-Pañeda.

Reprints and permissions information is available at <http://www.nature.com/reprints>

Publisher's note Springer Nature remains neutral with regard to jurisdictional claims in published maps and institutional affiliations.

Open Access This article is licensed under a Creative Commons Attribution 4.0 International License, which permits use, sharing, adaptation, distribution and reproduction in any medium or format, as long as you give appropriate credit to the original author(s) and the source, provide a link to the Creative Commons licence, and indicate if changes were made. The images or other third party material in this article are included in the article's Creative Commons licence, unless indicated otherwise in a credit line to the material. If material is not included in the article's Creative Commons licence and your intended use is not permitted by statutory regulation or exceeds the permitted use, you will need to obtain permission directly from the copyright holder. To view a copy of this licence, visit <http://creativecommons.org/licenses/by/4.0/>.

© The Author(s) 2025